Accepted Author Manuscript (AAM)

Article Title: Monitoring Photo-Fenton and Photo-Electro-Fenton process of contaminants emerging concern by a gas diffusion electrode using $Ca_{10-x}Fe_{x-y}W_y(PO_4)_6(OH)_2$ nanoparticles as heterogeneous catalyst

Authors: Fausto Eduardo Bimbi Júnior, Beatriz Tavoloni Marin, Leticia Mira, Carlos Henrique Magalhães Fernandes, Guilherme Vilalba Fortunato, Michell de Oliveira Almeida, Kathia Honório, Renata Colombo, Abner de Siervo, Marcos Roberto de Vasconcelos Lanza, Willyam Róger Padilha Barros

DOI: https://doi.org/10.1016/j.chemosphere.2024.142515

Journal: *Chemosphere*

Received date: 24 april 2024
Accepted date: 31 may 2024
Available online: 01 june 2024

Author Accepted Manuscript

Graphical Abstract

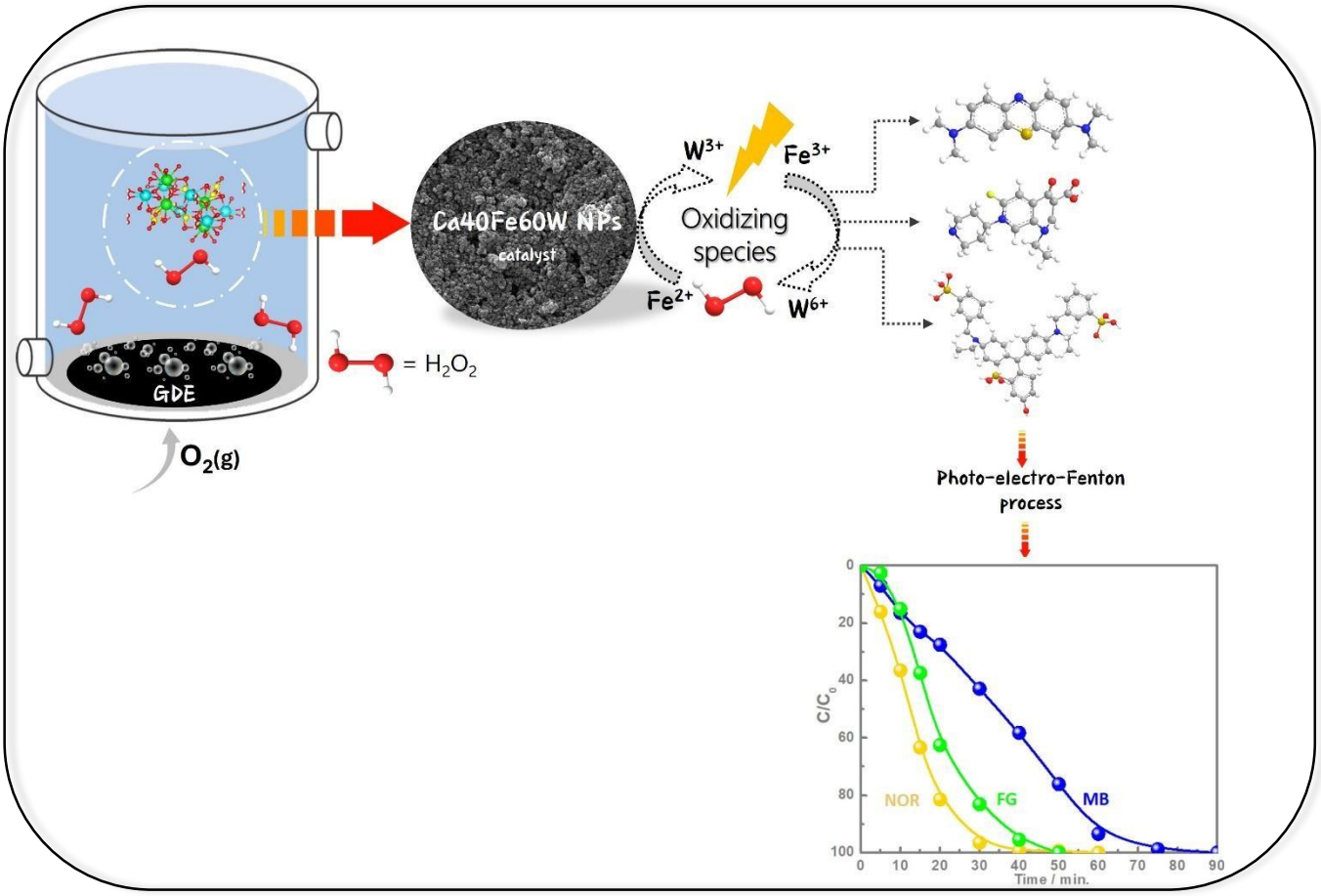

Monitoring Photo-Fenton and Photo-Electro-Fenton process of contaminants emerging concern by a gas diffusion electrode using $Ca_{10-x}Fe_{x-y}W_y(PO_4)_6(OH)_2$ nanoparticles as heterogeneous catalyst

Fausto E.B. Júnior[1,4], Beatriz T. Marin[1], Letícia Mira[1], Carlos H.M. Fernandes[1], Guilherme V. Fortunato[1], Michell O. Almeida[1], Kathia M. Honório[2], Renata Colombo[2], Abner de Siervo[3], Marcos R. V. Lanza[1*], Willyam R. P. Barros[4*]

[1]*São Carlos Instiute of Chemistry, University of São Paulo - USP, Avenida Trabalhador São Carlense 400, São Carlos, SP, 13566-590, Brazil*

[2]*School of Arts, Sciences and Humanities, University of São Paulo - EACH-USP, Rua Arlindo Béttio 1000, São Paulo, SP, 03828-000, Brazil*

[3]*Campinas Institute of Physics, State University of Campinas - UNICAMP, Sérgio Buarque de Holanda 777, Campinas, SP, 13083-859, Brazil*

[4]*Faculty of Exact Sciences and Technology, Federal University of Grande Dourados – UFGD, Rodovia Itahum Km 12, Dourados, MS, 79804-970, Brazil*

*Corresponding authors

Telephone: +55 67 3410-2174; +55 16 3373-8659

E-mail addresses: *willyambarros@ufgd.edu.br (W. R. P. Barros);*

marcoslanza@usp.br (M. R. V. Lanza)

ABSTRACT

The catalytic performance of modified hydroxyapatite nanoparticles, $Ca_{10-x}Fe_{x-y}W_y(PO_4)_6(OH)_2$, was applied for the degradation of methylene blue (MB), fast green FCF (FG) and norfloxacin (NOR). XPS analysis pointed to the successful partial replacement of Ca by Fe. Under photo-electro-Fenton process, the catalyst $Ca_4Fe^{II}_{1.92}W_{0.08}Fe^{III}_4(PO_4)_6(OH)_2$ was combined with UVC radiation and electrogenerated H_2O_2 in a Printex L6 carbon-based gas diffusion electrode. The application of only 10 mA cm^{-2} resulted in 100% discoloration of MB and FG dyes in 50 min. of treatment at pH 2.5, 7.0 and 9.0. The proposed treatment mechanism yielded maximum TOC removal of ~80% and high mineralization current efficiency of ~64%. Complete degradation of NOR was obtained in 40 min., and high mineralization of ~86% was recorded after 240 min. of treatment. Responses obtained from LC-ESI-MS/MS are in line with the theoretical Fukui indices and the ECOSAR data. The study enabled us to predict the main degradation route and the acute and chronic toxicity of the by-products formed during the contaminants degradation.

Keywords: Isomorphic substitution, iron oxide, Printex L6 carbon, hydroxyapatite nanoparticles, photo-electro-Fenton, emerging contaminants

1. Introduction

Hydroxyapatite ($Ca_{10}(PO_4)_6(OH)_2$) is a chemical compound that belongs to the class of apatites and whose chemical composition structure mainly consists of calcium (Ca) and phosphorus (P) ions. The variation in the composition of hydroxyapatite nanoparticles (HAp-NPs) is attributed to the difference in the ratio of Ca/P ions, which, in this case, is equal to 1.67. For this Ca/P ratio (1.67), the HAp-NPs present high physical stability and low solubility, which is not the case for other types/compositions of calcium phosphate (Ibrahim et al., 2020).

HAp-NPs have a high surface charge - due to the presence of Ca^{2+}, PO_4^{3-} and OH^- ions in its composition, and colloid-like properties, as well as a high capacity of adsorption of several emerging pollutants in aqueous media. Considering the high adsorption capacity of HAp–NPs, several studies conducted with the aim of exploring this chemical property of the compound have recorded good responses in terms of total phase separation of heavy metals (Ferri et al., 2019; Wang et al., 2019), dyes (Pai et al., 2021; Ragab et al., 2019) and proteins (Al-Ahmed et al., 2020; Nagasaki et al., 2017). Another interesting property of HAp-NPs is that the material can be used as a photocatalyst in reactions involving the degradation of organic pollutants due to the ability of Ca^{2+} ions to fluoresce, generating electrons in the medium (Edralin et al., 2017; Liu et al., 2016; Lv et al., 2024).

Through partial isomorphic substitution of Ca^{2+} with metal ions such as La^{3+}, Sm^{3+}, Gd^{3+}, Ho^{3+}, Yb^{3+}, Lu^{3+} (Cawthray et al., 2015), Mg^{2+} (Rasskazova et al., 2019), Ti^{2+} (Singh et al., 2020),Co^{2+} (Boukha et al., 2016), Fe^{2+} (Tampieri et al., 2012) and Fe^{3+} (Kabir et al., 2012), one can modify or fine-tune the properties of HAp-NPs and obtain a new, structurally improved material. Apart from improving the structural composition of HAp-NPs, partial isomorphic substitution of Ca^{2+} with any of the metal ions stated above

also helps enhance the catalytic efficiency of HAp-NPs when applied in photodegradation processes targeted at the treatment of contaminated matrices.

In terms of the partial isomorphic substitution of Ca^{2+} with Fe^{2+}/Fe^{3+} ions, in the form of iron oxide/iron hydroxide (*e.g.* Fe_3O_4,α-Fe_2O_3,γ-Fe_2O_3, α-FeOOH), in the HAp-NPs structure, and the incorporation of magnetism, the NPs can be used as a suitable catalyst for the degradation of organic compounds in Fenton and Photo-Fenton-like processes (Avakyan et al., 2021; Hou et al., 2016; Saber-Samandari et al., 2014; Valizadeh et al., 2014). Under the Fenton and Photo-Fenton oxidation mechanisms, the degradation process is favored by the $Fe^{2+/}Fe^{3+}$ redox cycle, with the decomposition of hydrogen peroxide (H_2O_2) (Eq. 1 and 2), and this process leads to the formation of hydroxyl radicals ($^{\bullet}OH$), which react with organic compounds (RH) (Eq. 3), oxidizing them partially or completely (Brillas, 2022; Nidheesh et al., 2023).

$$Fe^{2+}(aq) + H_2O_2(l) \rightarrow Fe^{3+}(aq) + {}^{\bullet}OH(aq) + OH^{-}(aq) \quad (1)$$

$$Fe^{3+}(aq) + H_2O(l) + h\nu \rightarrow Fe^{2+}(aq) + {}^{\bullet}OH(aq) + H^{+}(aq) \quad (2)$$

$$^{\bullet}OH(aq) + RH(aq) \rightarrow H_2O(l) + {}^{\bullet}R(aq) \quad (3)$$

Other partial isomorphic substitutions may occur via iron ions present in the octahedral sites of γ-Fe_2O_3/Fe_3O_4, which can also be replaced by transition metals (W^{6+}, V^{5+}, Cu^{2+}, Co^{2+}, Ni^{2+}, Sm^{3+}). In this case, co-catalytic effect occurs, and this helps to enhance the kinetics of pollutants degradation and decreases the energy related to the activation and formation of less stable by-products, resulting in the total mineralization of refractory organic contaminants to H_2O, CO_2 and inorganic salts (Alburaih et al., 2022; Barros et al., 2016; Deng et al., 2023; Kumar et al., 2023; Ma et al., 2021; Zhang et al., 2020).

In this sense, the use of heterogeneous catalysts with isomorphic substitution of transition metals is a viable treatment alternative in Fenton and Photo-Fenton-like

processes, especially when one employs Fe^{2+}/Fe^{3+} ions which confer high reactivity to the reaction, in addition to preserving/ensuring the magnetism of the NPs and enabling the recyclability of the catalysts. It should be noted that the displacement of a metallic cation by another of similar size can result in minimal changes in the primary crystalline structure of the catalyst (Kirchon et al., 2020).

To develop a highly efficient catalytic material endowed with all the aforementioned properties, in this present work, HAp-NPs were doped with Fe_3O_4 NPs and W^{6+} ions, and this gave rise to $Ca_{10-x}Fe_{x-y}W_y(PO_4)_6(OH)_2$, which was denoted shortly by CaFeW. The present study sought to investigate the effects arising from the modification of HAp-NPs and its use as heterogeneous catalysts in the degradation of three model molecules: cationic and anionic dyes (Methylene blue (MB), C.I. 52015 and Fast Green FCF (FG), C.I. 42053), and a drug from the fluoroquinolone class (Norfloxacin (NOR)).

The degradation processes were evaluated using the Photo-Fenton and Photo-Electro-Fenton, where the Photo-Electro-Fenton was applied in a system composed of a gas diffusion electrode (GDE) made from Printex L6 carbon (PCL6) - a carbonaceous material which contains oxygenated and nitrogenated functional groups.

The application of this proposed treatment strategy produced satisfactory results in terms of color removal, concentration decay and reduction of total organic carbon (TOC), in addition to a reduction in reaction time and in by-products toxicity.

2. Materials and Methods

2.1 Chemicals

The experiments were conducted using the following chemicals and reagents acquired from Sigma Aldrich (São Paulo - SP, Brazil): Calcium sulfate ($CaSO_4 \cdot 2H_2O$), phosphoric acid (H_3PO_4), ammonium hydroxide (NH_4OH), iron sulfate (II) heptahydrate

($FeSO_4 \cdot 7H_2O$), iron sulfate (III) pentahydrate ($Fe_2(SO_4)_3 \cdot 5H_2O$), sodium tungstate dihydrate ($Na_2WO_4 \cdot 2H_2O$), sodium hydroxide (NaOH), sodium borohydride ($NaBH_4$), potassium sulfate (K_2SO_4), potassium chloride (KCl), sulfuric acid (H_2SO_4), hydrogen peroxide (H_2O_2 (30% v/v)), ethyl alcohol (C_2H_6O) (70% v/v)), MB dye ($C_{16}H_{18}ClN_3S$), FG dye ($C_{37}H_{34}N_2O_{10}S_3$) and NOR ($C_{16}H_{18}FN_3O_3$). The remaining reagents employed in the experiments were of analytical grade and used without the need for additional purification. Ultrapure water from Millipore Milli-Q, with resistivity of 18.2 MΩ cm^{-1}, was used in the conduct of the experiments.

2.2 Synthesis of $Ca_{10-x}Fe_{x-y}W_y(PO_4)_6(OH)_2$ NPs

The HAp-NPs were synthesized using the co-precipitation method described by Bimbi Junior et al., 2022) [31]. For the modification of the NPs, the Ca^{2+} ion was replaced by Fe^{2+} ions in the following percentages: 40, 30, 25 and 0%. The NPs were denoted by Ca40Fe60W, Ca30Fe70W, Ca25Fe75W and Ca0Fe100W, as presented in Table S1.

Briefly, for the synthesis of Ca40Fe60W NPs – for example, 20 mmol of $CaSO_4 \cdot 2H_2O$, 0.4 mmol of $Na_2WO_4 \cdot 2H_2O$, 10 mmol of $FeSO_4 \cdot 7H_2O$ and 10 mmol of $Fe_2(SO_4)_3 \cdot 5H_2O$ were hydrated in 200 mL of ultrapure water at 25 °C using a mechanical stirrer for 25 min. After that, 2 mL of 0.5 mol L^{-1} $NaBH_4$ was added to the mixture as a reducing agent.

For the complete precipitation of the iron oxide NPs, 100 mL of 2.0 mol L^{-1} NaOH were added to the mixture in the presence of 1.5 mL of concentrated H_3PO_4; in order to maintain the pH level above 8.0, concentrated NH_4OH was applied. The temperature level was raised to 80 °C and the solution was subjected to stirring for 40 min. After this period (40 min.), the NPs produced were separated with a neodymium magnet, washed several times with ultrapure water and dried at 70 °C for 24 h. The other NPs compositions were

synthesized based on the aforementioned procedure, but with changes in the mass proportions (see Table S1).

2.3 Synthesis of PCL6-GDE

To manufacture the PCL6-based GDE, first, commercial PCL6 (acquired from Evonik®) was subjected to heat treatment, in which 2.0 g of carbon was homogenized in 100 mL of ultrapure water for 40 min., and the dispersion was then subjected to ultrasound treatment. The solution was subsequently transferred to an autoclave of 80 mL at 180° C, where it was kept for 24 h. At the end of this period, the PCL6 material was washed 3 times with ultrapure water and ethanol (C_2H_6O (70% v/v)) and was left to dry at 80 ºC for 12 h. After drying, 1.1 g of PCL6 and 0.46 g of polytetrafluoroethylene (PTFE) were placed in 30 mL C_2H_6O (70% v/v), where the mixture was subjected to ultrasound treatment in order to form an ink.

The ink was deposited on carbon fabric of 6.5 × 18.5 cm dimension and the material was dried in a muffle furnace at 120º C. After this period, another fabric was placed under the doped fabric and the material was subjected to pressing, where it remained under pressure of 0.5 atm at 260 °C for 10 min. At the end of this time, the GDE was cooled to room temperature and round electrodes measuring 6.0 cm in diameter were produced.

2.4 Instrumentation and Characterization

The morphology of the CaFeW NPs was analyzed using field emission gun – scanning electron microscopy with energy dispersive X-ray (SEM-FEG-EDX, JEOL, model JSM-7200F) and high-resolution transmission electron microscopy (HRTEM, FEI TECNAI G^2 F20). The phase analysis was conducted using X-ray diffraction (XRD, Bruker, D8 advance model). The local structures of the samples were characterized by X-ray photoelectron spectroscopy (XPS) using SPECS Phoibos 150 hemispherical analyzer

with multi-channeltron detection and Al Kα radiation (1486.6 eV), at a constant energy setting of 10 eV. The powdered samples were directly secured to a stainless-steel sample holder using carbon tape without any additional preparation. To fit the data, Lorentzian lines were used with Gaussian distribution, and a Shirley-type background was employed to account for the inelastic background contribution. The functional groups present in the NPs were analyzed using Fourier transform infrared (FTIR) spectroscopy (Jasco 4100 spectrophotometer). The analysis of the interaction of the surface charges of the CaFeW NPs with the reaction medium was carried out using the point of zero charge (pH_{PZC}) based on the eleven-point model (Kosmulski, 2020).

2.5 Analysis and Degradation Methods

2.5.1 Degradation of MB and FG Dyes Using the Photo-Fenton Process

The degradation of the MB and FG dyes through the Photo-Fenton process was conducted using a 250 mL glass reactor positioned inside a wooden box in order to eliminate any external interferences. 100 mL of 100 mg L^{-1} MB or FG dyes at pH 2.5, 7.0 and 9.0 were added to this reactor, where either 0.1 mol L^{-1} NaOH or 0.1 mol L^{-1} H_2SO_4 solution was used to adjust the pH values. The degradation was carried out under mechanical stirring at 20 °C for 2 h. The temperature of the reaction mixture was maintained by re-circulating cold water around the reactor. In each degradation process, 1,330 µL of H_2O_2 (30% v/v) and 0.13g of CaFeW NPs were employed. A 125 W mercury lamp, placed 9.0 cm away from the solution, was used as the UVA radiation source.

For the degradation analysis, different processes were carried out; these included (1) UVA only (Photolysis); (2) addition of H_2O_2 only; (3) NPs only (Adsorption); (4) H_2O_2 + NPs (Fenton); (5) UVA + NPs (Photocatalysis); (6) UVA + H_2O_2; and (7) UVA + H_2O_2 + NPs (Photo-Fenton).

The discoloration rate (Eq. 4) was evaluated using the Cary-50 UV-Vis spectrophotometer; the absorbance decay was monitored at 663 and 630 nm for the MB and FG dyes, respectively.

$$\text{Discoloration (\%)} = \left(\frac{\text{Abs}_{(0)} - \text{Abs}_{(t)}}{\text{Abs}_{(0)}}\right).100 \quad (4)$$

To optimize the results obtained under the Photo-Fenton process, degradation analyses (at pH 2.5) were carried out by varying the mass of the catalyst (0.66 to 2.00 g) and the volume of H_2O_2 (30% v/v) (660 to 2,000 µL).

In order to evaluate the stability of CaFeW NPs at pH 2.5, Fe^{2+} leaching was analyzed at the end of each Photo-Fenton experiment using the method described by the American Public Health Association (Krishna Murti et al., 1970).

2.5.2 H_2O_2 Electrogeneration Using PCL6-GDE

To determine the amount of H_2O_2 produced *in situ*, the following apparatus and conditions were employed: a glass electrochemical cell of 250 mL, placed under O_2(g) flow of 130 mL min^{-1} and subjected to mechanical agitation at 20 ºC. The electrochemical cell contained the following: the PCL6-GDE, used as working electrode, which was placed in contact with a stainless-steel screen in order to ensure electrical contact; Ag|AgCl (2.5 mol L^{-1} KCl) used as reference electrode; and platinized titanium used as counter electrode. An amount of 200 µL of electrolyte was collected at times 0, 5, 10, 15, 20, 30, 40, 50, 60, 75, 90 and 120 min. of reaction and complexed with 430 µL of ammonium molybdate ($(NH_4)_6Mo_7O_{24}$). The UV-Vis apparatus was used to determine the absorbance obtained via this experiment; and through calibration curve, the electrogenerated H_2O_2 concentration (C_{H2O2}) was determined. The energy consumption was calculated using Eq. 5.

$$\text{EC(\%)} = \frac{1000 \,.\, E_{cel} \,.\, t \,.\, I}{V \,.\, CH_2O_2} \quad (5)$$

EC = energy consumption

E_{cel} = cell potential
t = time (h)
I = current (A)
V = volume (L)

2.5.3 Degradation of MB, FG Dyes and NOR Using the Photo-Electro-Fenton Process

For the degradation of MB, FG dyes and NOR under the Photo-Electro-Fenton process, the optimized conditions of the catalyst mass were employed (described in section 2.5.1). The degradation analysis was conducted using a reactor containing the PCL6-GDE with a UVC radiation lamp (9 W) positioned inside it in a quartz tube. A thorough analysis was conducted in order to evaluate the influence of pH (2.5, 7.0 and 9.0), supporting electrolyte (0.1 mol L^{-1} K_2SO_4 and 0.1 mol L^{-1} KCl) and current density (10 and 20mA cm^{-2}) on the process involving the degradation of MB and FG dyes.

The analysis involving the degradation of NOR was also performed based on the optimized conditions stated in the procedure described above. It is worth noting however that here we evaluated the influence of NOR concentration (25, 50 and 100 mg L^{-1}), where the concentration decay was monitored by high-performance liquid chromatography (HPLC, SHIMADZU 20A) with LC-20AD and SPD-20AD pumps (UV-Vis detector). For this analysis, NOR concentration was monitored using a core shell C-18 reversed phase as the stationary phase (150 mm × 4.6 mm, 5 μm particle size, from Phenomenex®) and a mixture of 0.1% (*V*/*V*) formic acid solution and acetonitrile in the ratio 70:30 as the mobile phase (1.0 mL min^{-1}), in an isocratic mode. The injection volume, detection wavelength, and column temperature employed were 25 μL, 270 nm and 23°C, respectively.

The mineralization current efficiency (MCE) was calculated in all the Photo-Electro-Fenton experiments using Eq. 6, taking into account the total organic carbon (TOC, Shimadzu) measurements.

$$\text{MCE (\%)} = \left(\frac{n \,.\, F \,.\, V \,.\, \Delta TOC}{4.32.10^{7} \,.\, \text{m} \,.\, \text{i} \,.\, \text{t}}\right).100 \quad (6)$$

MCE = mineralization current efficiency
n = stoichiometric number of electrons transferred during mineralization
F = Faraday constant (96487 C mol^{-1})
V = volume (L)
ΔTOC = variation of total organic carbon (mg L^{-1})
m = number of carbons
I = current (A)
t = time (h)

The by-products of MB, FG dyes and NOR were identified by liquid chromatography coupled to electrospray mass spectrometry (LC-ESI-MS/MS). Chromatographic analyses were performed using a modular liquid chromatography system (Prominence LC 20 AT, Shimadzu, Kyoto, Japan). The chromatographic analyses of the contaminants were performed using Shim-pack GIST C18 column (150 mm × 4.6 mm × 5 µm). The mobile phase used for the analysis of MB and NOR was composed of water (solvent A) and acetonitrile (solvent B) acidified with 0.1% formic acid. The analysis of FG was performed using water acidified with 0.1% formic acid (solvent A) and acetonitrile (solvent B). The analyses were performed through the application of the following gradient elution program: 0-5 min: 10-37% B; 5-8 min: 37-100% B; and 8-10 min: 100-10% B, at a flow rate of 0.8 mL min^{-1}. Mass spectrometry analyses were performed using triple quadrupole equipment (LC/MS-8030, Shimadzu, Kyoto, Japan), operated in full scan mode with positive ionization. Temperatures of 250 and 400 °C were applied to the desolvation block and ion source, respectively. Nitrogen was used as nebulizer and desolvation gas at flow rates of 3 and 15 L min^{-1}, respectively.

2.5.4 Computational Simulations of NOR Degradation and Toxicity

Considering the high toxicity of NOR in aquatic environments and/or in wastewater, this molecule was chosen for the conduct of computational simulation tests

with the aim of evaluating its degree of toxicity after being subjected to degradation via the Electro-Fenton process.

Initially, the three-dimensional structure of the NOR molecule was constructed in the Avogadro 1.2 program. After that, conformation optimization was carried out in the Gaussian 09 program using the CAM-B3LYP density functional, with the basis function 6-31++G(3d,3p), and the medium was calculated using the implicit solvent conductor-like polarizable continuum model (CPCM) (water) (Marcus D Hanwell1, 2*, DonaldECurtis3, David C Lonie4, Tim Vandermeersch5, 2014). In addition to the geometric optimization of the molecule, the charges were calculated using the natural population analysis (NPA) method. After obtaining the optimized conformations of NOR, the energy values were calculated using the single point of the molecules with charge +1 and charge -1 (Wei et al., 2024). The charges were calculated in order to obtain Fukui indices (f^0), which are related to the radical attack. Based on Eq. 7, one can estimate the Fukui (f^0) indices (Vlahović et al., 2023):

$$f^0 = (q_{N-1} - q_{N+1})/2 \quad (7)$$

f^0= Fukui indices
q_{N-1}= molecule charge with a gain of 1 electron (a molecule with charge +1)
q_{N+1}= molecule charge with a loss of 1 electron (a molecule with charge -1)

Using the f^0 indices, one can predict the regions in a molecule that are susceptible to radical attacks, where a higher index value indicates a more reactive region.

After using the computational analyses of the Fukui indices to estimate the toxicity of NOR and the by-products recorded through mass spectrometry, the ecological structure activity relationships (ECOSAR) technique was used to predict the aquatic toxicity of fish, crustaceans, and green algae (Li et al., 2023). Under the ECOSAR method, structure-activity relationships (SAR) descriptors are used in linear regression; the method uses the

lethal concentration value of 50 (LC_{50}) for the analysis of acute toxicity in fish and daphnids over an exposure period of 96 and 48 h, respectively (Qutob et al., 2022). LC_{50} predicts the concentration of a substance required to kill 50% of the sample population in a determined period and within an aquatic environment. For green algae, the ECOSAR tool estimates the median effect concentration value of 50 (EC_{50}) for an exposure period of 96 h (Reuschenbach et al., 2008). Thus, given its efficiency in terms of toxicity assessment, the NOR molecule and all the by-products recorded through mass spectrometry were subjected to toxicity analysis using the ECOSAR method.

3. RESULTS AND DISCUSSION

3.1 Characterization of CaFeW NPs

X-ray diffraction (XRD) analyses were performed in order to evaluate the crystallographic planes present in the CaFeW NPs. Fig. 1A-D shows that all the CaFeW NPs exhibited two phases which corresponded to magnetite (Fe_3O_4) and $Ca_{10}(PO_4)_6(OH)_2$. The Fe_3O_4 crystallographic planes were associated with the red color in the following peaks: (220), (311), (222), (400), (422), (511) and (440), which corresponded to typical cubic inverse spinel (Yew et al., 2016). The $Ca_{10}(PO_4)_6(OH)_2$ crystallographic planes were represented by the black color related to the following peaks: (002), (211), (300), (202), (310), (222) and (213) (Indrani et al., 2017).

When the Ca^{2+} ions were replaced by Fe^{2+} ions in the synthesis of the CaFeW NPs, there was an increase in the intensity of the peaks corresponding to the $Ca_{10}(PO_4)_6(OH)_2$ structure; this pointed to a greater crystallinity of the NPs when the iron ions occupied the sites of the Ca^{2+} ions. A careful look at the CaFeW NPs showed that there was a structural modification in the structure of the material and not just a mere decoration; this is clearly seen in the crystallographic planes of the Ca0Fe100W NPs, where one will observe that even without Ca^{2+} ions in its composition, this material still

exhibited the same characteristic planes of the unmodified HAp-NPs. This is clearly indicative of the replacement of Ca^{2+} ions by Fe^{2+}/Fe^{3+} ions, where the crystallographic form was maintained. Another point that is worth mentioning is that the incorporation of W^{6+} ions into the Fe_3O_4 NPs structure did not lead to a distortion of the crystal planes; this evidently points to a successful isomorphic substitution.

The FTIR spectra in Fig. 1E-H show the bands corresponding to the vibrations of the PO_4^{3-} (at 569, 603, 803 and 1,047 cm^{-1}) and OH^- (at 3,432 cm^{-1}) groups (Collins Arun Prakash et al., 2020). The identification of the bands related to CO_3^{2-} (1,491; 1,560; and 1,641 cm^{-1}) points to its successful incorporation into the CaFeW NPs via the use of the non-inert atmosphere, leading to the formation of these NPs in the carbonated form (Youness et al., 2017). A low intensity band of Fe-O bond was identified at 444 cm^{-1}, indicating the presence of iron oxides (Mishra et al., 2014). Bands related to the bonds of W^{6+} ions were not observed; Ca0Fe100W NPs exhibited CO_3^{2-} bands, indicating the formation of iron carbonate in this composition.

A careful look at the SEM-FEG images of the CaFeW NPs (Fig. 1I-M) shows that the material exhibits a rough, irregular structural appearance, possibly due to high porosity, with smaller rounded particles on its surface, which are typically related to iron oxides, such as Fe_3O_4 (Chang and Jampang, 2023). An increase in the proportion of iron ions in the structure of the CaFeW NPs results in the formation of agglomerates with a more solid appearance, and this tends to diminish the structural roughness. The Ca0Fe100W NPs (Fig. 1I) can be found to exhibit rounded, agglomerated particles with round particles of smaller size on its surface (Fig. 1J). Even though these CaFeW NPs exhibit primarily common characteristics, none of them display the same profile in terms of particle disposition and shape, and this makes them follow different mechanisms when applied in the study of organic compounds degradation.

The atomic ratio percentage of calcium (Ca) and phosphorous (P) present in the CaFeW NPs structure obtained from the EDX analysis is shown in Table S2; as can be observed, the molar ratio obtained for Ca/P is 2.33 ± 0.12; considering that the $Ca_{10}(PO_4)_6(OH)_2$ has a limiting stoichiometry of 1.67, this increase may be attributed to the carbonation of the material during the synthesis. The Ca0Fe100W NPs exhibited phosphorus ions in the structural composition; this points to a combination of the material with iron ions.

Based on a careful inspection of the structure of Ca40Fe60W NPs by HRTEM (Fig. 2), the material was found to exhibit a crystalline profile through the analysis of bright field (Fig. 2A) and dark field (Fig. 2A1).

Through the application of the energy dispersive spectroscopy (EDS) technique, the atomic percentage of each element present in the Ca40Fe60W NPs was obtained - Fig. 2A2. The atomic percentage values obtained were: 3.7% of P, 25.0% of Fe, 64.0% of O, 0.2% of W and 7.1% of Ca. As per the theoretical value used in the synthesis (60% Fe with 40% Ca), the ratio obtained was approximately 78% Fe to 22% Ca. This variation in atomic ratio percentage may be attributed to the non-homogeneous dispersion of Fe_3O_4 NPs, which causes a change in the atomic percentage values, based on the area investigated. Thus, the crystalline planes were thoroughly evaluated, and the result obtained from this analysis pointed to a predominance of planes 311 (Fig. 2B) and 211 (Fig. 2B1), where the crystalline planes of greater intensity corresponded to Fe_3O_4 and hydroxyapatite NPs, respectively, as observed in the XRD data (Patel et al., 2015).

The TEM images in Fig. 2C-F show the morphology of the CaFeW NPs; as can be observed, all the compositions of the material can be found to exhibit round (Fe_3O_4 NPs) and agglomerated particles, with an irregularly-shaped plate on the surface. It is also noted that even for the Ca0Fe100W NPs, structures like hydroxyapatite NPs are

clearly observed; this points to the replacement of Ca^{2+} ions by Fe^{2+}/Fe^{3+} ions, and thus confirms the data obtained from the XRD analysis.

XPS analyses were performed in order to have a comprehensive knowledge of the surface composition and determine the atomic composition of the different elements present in each sample; Fig. S1 shows the survey spectra obtained for all the nanoparticles. In general, the survey spectra of all the materials were found to exhibit the characteristic peaks of hydroxyapatite NPs, which correspond to O 1s, P 2p, Ca 2p, and C 1s core levels at the average positions of 534, 136, 350, and 287 eV, respectively. The presence of C in the spectra is associated with surface contamination, which is likely related to calcium carbonates and probable adventitious carbon species. Interestingly, the survey spectrum of the Ca0Fe100W NPs - where Ca was replaced by Fe, did not exhibit any peaks related to Ca; in addition, the spectrum showed a decrease in intensity of the C 1s peak, as expected. The presence of iron peaks (Fe 2p at ca. 710 eV) and Auger peaks at higher binding energies pointed to the successful incorporation of Fe_3O_4 NPs in all the samples. Due to its low quantity and high dispersibility, W was only observed in the Ca0Fe100W NPs. The absence of other elemental peaks suggests the absence of foreign dopants. XPS analysis was performed in order to evaluate the elemental composition of the samples (Table 1). The results obtained showed that the atomic percentages closely approximated the theoretical values anticipated based on the nominal formula, as outlined in Table S1. For instance, in the case of Ca40Fe60W, one would expect an atomic composition of Ca ~9%, Fe ~13%, P ~13% and O ~63%, according to the nominal formula. Remarkably, the XPS results revealed values quite consistent with this theoretical composition, with Ca at approximately 12%, Fe at ca. 12%, P at ca. 7% and O at ca. 71%. These values are also found to be in good agreement with the EDX data obtained for the Ca and P elements (c.f. Table S2).

Fig. 3 shows the high-resolution (HR) XPS spectra for the O 1s, P 2p, Fe 2p regions. In general, for the Ca40Fe60W, Ca30Fe70W, and Ca25Fe75W NPs, the O 1s region can be deconvoluted into 5 distinct peaks, corresponding to specific chemical states; these states were identified as O-H, O-Fe and C=O, P-O, C-O and P-O-P, and adsorbed H_2O, located at energy levels of ~530.2, ~531.0, ~532.0, ~533.3 and ~534.4 eV, respectively. In all the NPs samples investigated, there was a substantial presence of P-O and P-O-P oxygen bonds - which are found to be typically characteristic of the lattice of HAp-NPs - in relatively higher proportions (as shown in Table S3). It is worth noting however that the Ca0Fe100W NPs exhibited a distinct profile with significant contributions from P-O and P-O-P oxygen bonds; furthermore, this sample exhibited a higher content of Fe-O oxygen bonds, which points to the coexistence of different oxygen chemical states, likely associated with the iron phosphate and Fe_3O_4 structures within the sample.

The HR XPS spectra in the P 2p region provided us with valuable insights into the chemical state of phosphorus within each sample. In the case of the Ca40Fe60W, Ca30Fe70W and Ca25Fe75W NPs, the region exhibited four distinguishable peaks corresponding to PO_4^{3-} ion, presumably Ca phosphate and iron phosphate states, with $2p_{3/2}$ and $2p_{1/2}$ spin-orbit components appearing at energy levels of 133.0 and 134.0 eV, as well as 135.1 and 136.0 eV, respectively. These spectral features are found to be closely in line with the chemical characteristics of HAp-NPs and point to the presence of the $FePO_4$ phase, albeit in minor amounts as indicated in Table S3; in essence, this clearly confirms the coexistence of the compounds within the NPs investigated (Barbaux et al., 1992).

In the Fe 2p region of all the samples, the HR XPS spectra exhibited a consistent pattern, allowing for deconvolution into 6 doublets with 2 X-ray satellites. Among these doublets, two were identified at binding energies of approximately 712 and 725 eV, along

with another pair at 714 and 728 eV. These doublets corresponded to the $2p_{3/2}$ and $2p_{1/2}$ spin-orbit components, which are typically indicative of Fe^{3+} species, and are commonly associated with γ-Fe_2O_3 and $FePO_4$ phases. The average concentrations of γ-Fe_2O_3 and $FePO_4$ were estimated at approximately 48 and 14%, respectively. However, it is noteworthy that due to the presence of mixed valence iron oxide phases, distinguishing between the contributions of Fe^{3+} and Fe^{2+} within the Fe_3O_4 phase was unfeasible. This challenge arises from the overlapping binding energies of the two iron species present within these mixed phases.

The HR XPS spectra related to the Ca 2p region (Fig. S2A) for all the samples revealed distinct features that were successfully deconvoluted. These spectra exhibited 2 X-ray satellites and 2 doublets positioned at average binding energies of 339 and 343 eV, 348 and 351 eV, and 349 and 353 eV. The two doublets were associated with the spin-orbital components of two distinct Ca^{2+} species. The first Ca^{2+} species could be linked to the presence of CO_3^{2-} ion, stemming from carbon impurities on the surface. The second Ca^{2+} species corresponded to the hexagonal phase typically encountered in HAp-NPs. Notably, the hexagonal Ca^{2+} species were found in higher proportions within the NPs, indicating their prevalence in the hydroxyapatite structure (Uskoković, 2020).

In general, the HR XPS spectra related to the C 1s region for all the samples (Fig. S2B) revealed the presence of carbon species from adventitious carbon, originating from the atmosphere, as well as C=O and O-C=O bonds which are likely related to carboxyl and carbonate groups present in the NPs (Uskoković, 2020).

For W present in low quantity and in wide distribution, the presence of this atom was only noticeable in the Ca0Fe100W NPs. Despite a very low signal-to-noise ratio, the HR XPS spectrum for W 4f (Fig. S2C) was deconvoluted into a doublet, which was

attributed to the $4f_{7/2}$ and $4f_{5/2}$ spin-orbit components of WO_3 chemical state; essentially, this points to the successful doping of the nanoparticles with W.

Fig. S3 shows the pH_{PZC} analysis conducted for the NPs; the pH range employed was 8.2 - 9.4. At pH value below the pH range, the catalytic charge on the CaFeW NPs surface is negative; at pH value above the range, the charge is positive; at pH value within the range, the charge is neutral. The results obtained showed that an increase in the Fe_3O_4 and W^{6+} dopant proportion led to a slight increase in the pH_{PZC} values; this outcome points to the addition of a greater number of metals in the structure of the NPs containing a higher proportion of dopants relative to those with a lower proportion of dopants.

3.2 Evaluation of the Photo-Fenton Process in the Degradation of MB and FG Dyes

The Photo-Fenton process was applied for the degradation (dye color removal) of MB and FG dyes using Ca40Fe60W, Ca30Fe70W, Ca25Fe75W and Ca0Fe100W NPs as heterogeneous catalysts at pH 2.5, 7.0 and 9.0. Based on this analysis, the best result in terms of MB dye color removal was obtained at pH 2.5 (Fig S4A), where 100% degradation was obtained for all the NPs investigated, with the exception of Ca25Fe75W (51.1%). The low removal rate recorded for the Ca25Fe75W may be attributed to the low Ca/Fe ratio in its structure, as this tends to decrease the synergism between the oxidation processes involved in the degradation of the material. The high dye color removal rate observed can be attributed to the Fenton process operating in combination with the photocatalysis of the unmodified HAp-NPs; this oxidation mechanism accelerates the formation of $^{\bullet}OH$, as can be observed in Eq. 8-12 (Expósito et al., 2017; Liu et al., 2021). In this case, the regeneration of Fe^{2+} ions favor the attack on the MB dye molecule through the constant production of oxidizing species, mainly $^{\bullet}OH$.

$$Fe^{II}(aq) + H_2O_2(aq) + H^+(aq) \rightarrow Fe^{III}(aq) + H_2O(l) + {}^{\bullet}OH(aq) \quad (8)$$

$$Fe^{III}(aq) + H_2O_2(aq) \rightarrow Fe^{II}(aq) + H^+(aq) + HO_2{}^{\bullet}(aq) \quad (9)$$

$Fe^{2+}(aq) + H_2O_2(aq) \rightarrow Fe^{3+}(aq) + {}^{\bullet}OH(aq) + OH^{-}(aq)$ (10)

$Fe^{3+}(aq) + H_2O(l) \rightarrow (FeOH)^{2+}(aq) + H^{+}(aq)$ (11)

$(FeOH)^{2+}(aq) + h\nu \rightarrow Fe^{2+}(aq) + {}^{\bullet}OH(aq)$ (12)

The Photo-Fenton process occurs through a co-catalyzed reaction, in the presence of W^{6+} ions; this process leads to the generation of a redox pair (Eq. 13), and contributes to the production of ${}^{\bullet}OH$ while decreasing the stability of the complexes and by-products formed (Zhou et al., 2019).

$${}^{o}W^{6+}\text{-}OH(aq) + H_2O_2(l) \rightarrow {}^{o}W^{n+}\ (n= 3, 4,5)\text{-}OH(aq) + {}^{\bullet}OH\ (aq) + OH^{-}(aq)$$ (13)

At pH 7.0 (Fig.S4B), there is a neutrality of charges on the NPs surface, as shown in the pH_{PZC} data; the application of this pH level on Ca40Fe60W NPs results in 92% of color removal. At pH 9.0 (Fig. S4C), there is a predominance of negative charges, and this leads to the emergence of an attraction force between the medium and the CaFeW NPs surface; this facilitates the interaction between the catalyst and the dye solution, promoting 100% of color removal when applied to the Ca40Fe60W NPs. It is worth noting that the color removal kinetics at alkaline pH is relatively slower; this is probably because of high concentration of OH^- ions in the solution which acts as a passivator of iron ions, forming iron hydroxide or oxide (Eq. 14) and decreasing the catalytic efficiency of the alkaline pH compared to pH 2.5.

$Fe^{3+}(aq) + 3\ OH^{-}(aq) \rightarrow Fe(OH)_3(s)$ (14)

Complementary data related to the degradation of the MB dye obtained from the application of other degradation processes (only H_2O_2, H_2O_2 + UVA, adsorption, photolysis, photocatalysis and Fenton) are presented in Fig. S5.

Regarding the degradation of the MB dye, the results obtained showed that the Ca40Fe60W NPs recorded the best overall results under all the pH values investigated when the Photo-Fenton process is executed at pH 2.5; thus, this composition was chosen

for the analysis of the optimization parameters of the process, taking into account the influence of catalyst mass and volume of H_2O_2 (30% v/v), as shown in Fig. S6.

The use of the lowest catalyst mass of 0.06g and H_2O_2 volume (30% v/v) of 660 µL in the MB dye degradation process was found to accelerate the color removal from 120 to 60 min. The analysis of the radiation source showed that the use of 15cm×15cm mirrored plates increases the reaction kinetics, since a greater amount of $^{\bullet}OH$ is produced through the breakdown of aqua complexes and H_2O_2 bonds caused by an increase in radiation, as can be observed in Eq. 15 (Mandavgane, 2020).

$$H_2O_2(aq) + h\nu \rightarrow 2^{\bullet}OH(aq) \quad (15)$$

In optimized conditions, the application of the Ca40Fe60W NPs under the Photo-Fenton process and in the presence of UVA radiation (125 W) resulted in the total organic carbon (TOC) removal (mineralization efficiency) of 89.7, 62.8 and 79.3% at pH 2.5, 7.0 and 9.0, respectively. These results point to the influence of the difference in force of attraction between the medium and the NPs surface, as observed by the data from the pH_{PZC} and the MB dye color removal. Another possible cause of incomplete mineralization is the formation of recalcitrant by-products, which hinder the $^{\bullet}OH$ action in the degradation process.

To evaluate the stability of CaFeW NPs, Fe^{2+} ions-leaching tests (Table S4) were performed at pH 2.5, 7.0 and 9.0. The results obtained showed that, at pH 2.5, there was leaching of 18.4, 13.7, 31.3 and 81.8 mg L^{-1} of Fe^{2+} ions when Ca40Fe60W, Ca30Fe70W, Ca25Fe75W and Ca0Fe100W NPs were applied, respectively. However, no leaching was detected at pH 7.0 and 9.0; this is clearly indicative of the stability of the NPs at less acidic pH. In this sense, the structural instability of NPs is found to be linked to the excess of H^+ ions present in the solution at pH 2.5, which causes a greater interaction with the

CO_3^{2-} ions, resulting in the partial solubilization of ferrous ions bicarbonate-complex, as shown in Eq. 16 (Guinotte et al., 1995).

$$FeCO_3(s) + H^+(aq) \rightarrow Fe^{2+}(aq) + HCO_3^-(aq) \quad (16)$$

The Fe^{2+} ions-leaching in carbonated form at pH 2.5 occurs only in the first cycle of degradation. However, when the NPs are reutilized, no leaching of iron ions is observed anymore; this shows that the CaFeW NPs become stable after decarbonation.

3.3 Study of H_2O_2 Electrogeneration Using PCL6-GDE

The analysis of H_2O_2 electrogeneration *in situ* was conducted based on the application of the PCL6-GDE under oxygen flow (130 mL min^{-1}) at pH 2.5, 7.0 and 9.0, and at current densities of 10 and 20 mA cm^{-2}, as seen in Fig. S7.

As shown in Fig. S7A, the application of the current density of 10 mA cm^{-2} at pH 2.5, 7.0 and 9.0 led to the electrogeneration of 377, 305 and 343 mg L^{-1} H_2O_2, respectively, after 120 min. of electrolysis. On the other hand, the application of 20 mA cm^{-2} (Fig. S7B) at pH 2.5, 7.0 and 9.0 resulted in the electrogeneration of 808, 744 and 654 mg L^{-1} H_2O_2. The low amount of H_2O_2 electrogenerated at pH 9.0 may be associated with low concentration of H^+ ions; this is because an increase in pH leads to a decrease in H_2O_2 electrogeneration. The effect of H^+ ions can be seen in Eq. 17, where the oxygen reduction reaction (ORR) via $2e^-$ is dependent on the H^+ concentration in the media (Bhuvanendran et al., 2022).

$$O_2(g) + 2H^+(aq) + 2e^- \rightarrow H_2O_2(aq) \quad (17)$$

For the analysis of energy consumption (Fig. S7C and Fig. S7D), the current density of 10 mA cm^{-2} was found to be more economical compared to the current density of 20 mA cm^{-2}; at 10 mA cm^{-2}, EC values of 22.5, 21.0 and 18.0 KWh Kg^{-1} were recorded as opposed to 32.0, 37.0 and 28.0 KWh Kg^{-1} recorded at 20 mA cm^{-2} in acidic, neutral, and alkaline media, respectively.

The H_2O_2 electrogenerated was activated in the Photo-Electro-Fenton process by the Ca40Fe60W NPs, where $^{\bullet}OH$ was produced, as seen in Eq. 7. It should be noted however that the regeneration ratio of the Fe^{2+}/Fe^{3+} catalytic cycle was lower than the H_2O_2 production; Eq. 8 was thus predominant in the degradation system. In this way, in electronic terms, Eq. 18 can be found to occur in the process.

$$Fe^{3+}(aq) + e^- \rightarrow Fe^{2+}(aq) \quad (18)$$

3.4 Using the Photo-Electro-Fenton Process for the Degradation of MB, FG Dyes and NOR

The Photo-Electro-Fenton process was applied for the degradation of MB, FG dyes and NOR using the PCL6-GDE reactor evaluated in the *in situ* production of H_2O_2. The experimental conditions employed included the following: 0.1 mol L^{-1} K_2SO_4 (electrolyte), 0.06 g of Ca40Fe60WNPs (heterogeneous catalyst), O_2 flow (130 mL min^{-1}), current density of 10 and 20 mA cm^{-2}, and pH 2.5, 7.0 and 9.0.

As can be seen in Fig. 4A and Fig. 4B, the application of pH 2.5 resulted in the highest degradation of the MB dye in the shortest period; total degradation was also obtained under all the conditions investigated after 90 min. of electrolysis. Regarding the mineralization analysis for the pH 2.5, 7.0 and 9.0, Fig. 4C and Fig. 4D show that the application of the current densities of 10 and 20 mA cm^{-2} resulted in the mineralization percentages ranging between 56.5% ± 10.55 and 61.55% ± 4.85, respectively. These results point to the partial mineralization of the MB dye and indicate the formation of recalcitrant by-products, with stabilization in the mineralization percentage after 30 min. of reaction.

To evaluate the influence of the electrolyte, namely, 0.1 mol L^{-1} K_2SO_4 and 0.1 mol L^{-1} KCl, in the MB dye degradation at pH 2.5, the Photo-Electro-Fenton process was applied at the current density of 20 mA cm^{-2} using Ca40Fe60W NPs as catalyst – see the results in Fig. S8A - Fig. S8C. Fig. S8A shows that both electrolytes recorded similar

results in terms of color removal, mineralization (Fig. S8B) and energy consumption (Fig. S8C); essentially, the results show that the Cl^- or SO_4^{2-} species act in a similar way in the process involving the indirect degradation of the MB dye. Thus, 0.1 mol L^{-1} K_2SO_4 was chosen as the optimal electrolyte for the conduct of other degradation experiments.

The FG dye (anionic dye) degradation process was also evaluated – see the results in Fig. 5A and Fig. 5B. As can be noted, the application of pH 7.0 and 9.0 resulted in higher color removal kinetics compared to pH 2.5 under both applied current densities (10 mA cm^{-2} and 20 mA cm^{-2}); this is clearly opposite to the results obtained in the MB dye degradation process. This different outcome is attributed to the difference in charges presented by the dyes; in addition, there were greater interactions between the CaFeW NPs surface and the compounds at opposite pH values, as observed from the pH_{PZC} data. Furthermore, a total FG dye color removal was recorded in 90 min. of electrolysis under all the experimental conditions investigated.

The results obtained from the analysis of FG dye mineralization under the Photo-Electro-Fenton process showed that the application of the current densities of 10 mA cm^{-2} (Fig. 5C) and 20 mA cm^{-2} (Fig. 5D) resulted in the average mineralization percentages of 76.45% ± 12.75 and 77.65% ± 8.05, respectively, at pH 2.5, 7.0 and 9.0. The results obtained showed an increasing pattern of mineralization, where constant increasing rates of FG dye degradation were recorded over the period of 120 min. of reaction. Fig. S9 presents complementary data related to FG dye degradation under the application of the following treatment processes: Photo-Fenton; Fenton; Photocatalysis; H_2O_2 + UVA; Photolysis; and Adsorption.

In general, the best conditions for Photo-Electro-Fenton degradation using Ca40Fe60W NPs as catalyst were as follows: pH 2.5; 0.1 mol L^{-1} K_2SO_4 as electrolyte;

and current density of 10 mA cm^{-2}. The application of these conditions led to the highest mineralization of MB and FG dyes with relatively lower costs of H_2O_2 electrogeneration.

For the analysis of the complete mineralization of MB and FG dyes (Eq. 19 and 20), the mineralization current efficiency (M.C.E %) was evaluated based on the application of the Photo-Electro-Fenton process in 120 min. (Domingo-Torner et al., 2023).

$$[C_{16}H_{18}N_3S]^+(aq) + 45\ H_2O(l) \rightarrow 16\ CO_2(g) + 3\ NO_3^-(aq) + SO_4^{2-}(aq) + 108\ H^+(aq) + 102e^- \quad (19)$$

$$[C_{37}H_{34}N_2O_{10}S_3]^{2-}(aq) + 82\ H_2O(l) \rightarrow 37\ CO_2(g) + 2\ NO_3^-(aq) + 3\ SO_4^{2-}(aq) + 198\ H^+(aq) + 192\ e^- \quad (20)$$

Table S5 shows the M.C.E values obtained in the degradation of MB and FG dyes. For the degradation of the MB and FG dyes, the application of current densities of 10 and 20 mA cm^{-2} at pH 2.5, 7.0, 9.0 yielded average M.C.E. values of 47.75% ± 7.26 and 54.78% ± 4.32, respectively, for the MB dye and 56.25% ± 5.83 and 55.38% ± 9.23, respectively, for the FG dye. Based on these results, one concludes that when it comes to the degradation of the MB and FG dyes, the current density of 10 mA cm^{-2} is clearly more recommended; this is because the application of this current density involved less energy consumption compared to the density of 20 mA cm^{-2}, though both recorded slightly similar M.C.E.

The degradation of NOR (25, 50 and 100 mg L^{-1}) was performed under optimized conditions based on the application of the Photo-Electro-Fenton process in an exhaustive electrolysis of 240 min. duration. Fig. 6A shows the NOR removal rate obtained following the application of HPLC; as can be noted, the NOR molecule was completely degraded after only 40 min. of electrolysis. As can be seen in Fig. 6B, the application of the Photo-Electro-Fenton process for NOR degradation yielded high mineralization rates,

with maximum mineralization of ~86% ± 0.80; the results obtained point to the suitability of the Photo-Electro-Fenton process as a highly promising technique for NOR mineralization. The results also showed that after 90 min. of electrolysis, there was a stabilization of the mineralization rates recorded for all the NOR concentrations investigated; this stabilization is linked to the formation of more stable species/by-products which are clearly very difficult to mineralize.

To estimate the M.C.E for NOR degradation, the Photo-Electro-Fenton process was carried out at pH 2.5, with current density of 10 mA cm^{-2}; the calculation was done based on Eq. 21 below.

$$C_{16}H_{18}FN_3O_3 + 38\ H_2O(l) \rightarrow 16\ CO_2(g) + 3\ NO_3^-(aq) + F^-(aq) + 94\ H^+(aq) + 90\ e^- \quad (21)$$

The experiments performed using NOR concentrations of 25, 50 and 100 mg L^{-1} yielded TOC removal rates of 62.6, 58.7 and 50.7%, respectively. The results obtained showed that the application of pH 2.5 yielded the best results in terms of NOR removal and energy consumption efficiency.

The recyclability test of the catalyst applied to the NOR degradation was also carried out, as shown in Fig. 6C. Ca40Fe60W NPs presented high catalytic performance during five consecutive runs when applied to the Photo-Electro-Fenton process, with no loss of activity during the electrolysis.

In general, Scheme S1 shows the degradation pathway of the compounds, i.e., the attack by radicals formed during electrolysis by the catalytic cycle (redox pair) of the Fe^{2+}/Fe^{3+} and W^{3+}/W^{6+} species.

Considering that the MB and FG dyes and NOR degradation processes did not lead to 100% mineralization, due to the formation of possible by-products, a study was conducted using LC-ESI-MS/MS in order to gain a comprehensible understanding on the degradation mechanism/pathway.

3.5 By-products Analysis from degradation of MB, FG dyes and NOR under the Photo-Electro-Fenton Process

The results obtained from the LC-MS/MS analyses show that the different conditions employed in the study did not influence the degradation pathway of the contaminants investigated. In general, the same degradation by-products were observed at different times, concentrations and/or pH applied. The degradation pathway identified showed that the degradation mechanism occurs through different means of $^{\bullet}OH$ attack on the molecules and the transformation reactions generate different by-products, including recalcitrant compounds that are not degraded even after the maximum electrolysis time.

The identification of the by-products was performed based on the molecular ion and characteristic fragments obtained from LC-MS/MS analyses and from previous studies on MB and FG dyes and NOR degradation reported in the literature.

3.5.1 MB Dye

Regarding the MB dye degradation, ten intermediate products related to the dye were detected (Table S6); the proposed degradation pathway is presented in Fig. 7.

The mechanism involving the degradation of the MB dye molecule under the Photo-Electro-Fenton process corroborate with the main pathway of attack of $^{\bullet}OH$ reported in other studies: disruption of the N–CH_3 bond, which has the lowest bond energy (70.8 $kcalmol^{-1}$); oxidation of –CH_3 groups; oxidation of the Cl-S bond in S=O and its attraction toward the cationic sulfur group and heteroaromatic ring, provoking the desulfonation or opening of the central aromatic ring (Awais et al., 2022; Khan et al., 2022; Kishor et al., 2021; Mrunal et al., 2019; Sithole et al., 2020; Wang et al., 2022).

After the aqueous dissolution of the MB dye, ionization of Cl to Cl^- occurs, generating the corresponding counter ion **1** (*m/z* 284) (Mrunal et al., 2019; Plater, 2003; Wang et al., 2022). Partial isomerization of **1** and •OH attack of methyl groups lead to the formation of product **8** (*m/z* 288) (Khan et al., 2022; Plater, 2003; Wang et al., 2022).

The demethylation of by-product **1** is the proposed pathway for the formation of derivatives **4** (*m/z* 244) and **10** (*m/z* 227) (Khan et al., 2022; Plater, 2003; Wang et al., 2022). Through the formation of product **4**, demethylation is accompanied by methyl group oxidation to HCHO, with the removal of -CH_4O. For product **10**, in addition to demethylation, there is also the loss of N-methylmethanamine group. The continued process of demethylation, followed by desulfonation in product **10,** leads to the formation of product **3** (*m/z* 183) (Awais et al., 2022; Mrunal et al., 2019).

Another degradation attack of •OH on MB molecule is linked to the benzene ring and the formation of polyhydroxy compounds, as well as nitrogen hydration on the aniline ring (Kishor et al., 2021; Plater, 2003; Wang et al., 2022). The conditions employed in the Photo-Electro-Fenton process promoted this pathway of attack on by-product **4,** leading to the formation of hydroxylated intermediate product **5** (*m/z* 343) and the hydroxylated and sulfoxide by-product **7** (m/z 263)

By-product **6** is generated through the nitrogen dehydration of the aniline ring and the adjacent ring opening, with the removal of the C_2H_6 group (Awais et al., 2022; Khan et al., 2022; Kishor et al., 2021; Plater, 2003; Wang et al., 2022). By-product **9** (*m/z* 115) is derived from the destruction of the C-S bond of thionine molecule in product **7** and the opening of the rings. The oxidation of the sulfoxide group to sulfone leads to the generation of the derivative **2** (*m/z* 143) (Awais et al., 2022; Khan et al., 2022; Kishor et al., 2021; Plater, 2003; Wang et al., 2022).

3.5.2 FG Dye

For the degradation of the FG dye, nine by-products (Table S7) were identified, based on the data shown in Fig. 8. The proposed degradation pathway involves the elimination of SO_4^{2-} and the breakdown of the bonds between the benzene rings via the

•OH species attack. This proposed degradation pathway is in line with the FG dye degradation mechanisms previously reported in the literature (Raducan et al., 2022).

The formation of by-products **4** (*m/z* 444), **5** (*m/z* 383) and **7** (*m/z* 523) occurred as a result of the loss of the C_2H_6 and SO_3^- groups, accompanied by the loss of methylbenzene-sulfonate, ethyl-phenylamino-methylbenzene-sulfonate and ethylamino-methylbenzene-sulfonate, respectively.

The •OH attack on benzene sulfonate fraction of product **5** leads to the formation of by-product **1** (*m/z* 304). The central C=C bond oxidation and the subsequent loss of the SO_3^- and benzenediol groups loss lead to the formation of product **3** (*m/z* 354) (Raducan et al., 2022). The formation of intermediate **2** (*m/z* 263) occurs as a result of the dehydration of product **7** and the loss of the benzenediol and methylbenzenediol groups.

The proposed pathway for the formation of compound **8** (*m/z* 531) involves the oxidation of CH_3 groups and the subsequent removal of the SO_3^- fraction from the FG dye molecule. Regarding compound **6** (*m/z* 425), its by-product precursor - compound **8,** undergoes oxidative process, and this leads to the loss of $-C_6H_6$ and $-CH_4O$ groups. The same pathway is suggested regarding the formation of compound 9 (*m/z* 227); this pathway involves the breakdown of the $-C_6H_8O$ group.

3.5.3 NOR

The NOR degradation process occurs via three main pathways of •OH attack (dihydroxylation; quinolone group and N-ethyl-quinolone side chain transformations; and piperazinyl ring transformation), accompanied or not by the defuorination process. For the NOR degradation process, a total of 14 by-products were identified and degradation pathways were put forward according to the proposed molecular structure (Fig. 9). The mass spectra data are presented in Table S8.

Dehydroxylation reaction was observed in the NOR molecule, with the formation of by-product **6** (*m/z*304), characterized by the loss of OH^- (17 Da) (Coledam et al., 2016; Jin et al., 2019; Sánchez-Montes et al., 2018). By-product 6 may have undergone decomposition through the loss of fluorine unit, giving rise to by-product **9** (*m/z* 273).

Piperazinyl ring oxidation generated intermediate **13**, identified in the protonated form *m/z* 336 (+16 Da) (Babić et al., 2013; Ding et al., 2017). The defluorination of compound **13** is the possible pathway for the formation of intermediate **3** (*m/z* 318). The pathway for the formation of compound **5** (*m/z* 279) may have involved the loss of C_2H_5NO (-59 Da) and the oxidation of N-methyl-piperazine, coupled with the loss of CH_3 (-15 Da) (Zhang et al., 2021). The loss of C_2H_5NO, the oxidation of N-methyl-piperazine oxidation and the transformation of the side chain of **3** lead to the generation of by-product **1** (*m/z* 291) (Sánchez-Montes et al., 2018).

An alternative pathway for the formation of intermediate **9** may have involved the dehydration of compound **1** (-18 Da, corresponding to the loss of H_2O). The loss of the methyl group from compound **9** as a result of oxidative rearrangements on the N-ethyl-piperazine side chain lead to the formation of by-product **12** (*m/z* 259). Studies reported in the literature have shown that •OH can attack the C=C bond of the quinolone group, leading to oxidation, cleavage, and ring degradation (Carneiro et al., 2020; Coledam et al., 2016; Ding et al., 2017; Liu et al., 2022; Sánchez-Montes et al., 2018; Wang et al., 2021); the protonated forms of by-product **11** (*m/z* 354) are expected to be generated by this stepwise degradation. The subsequent decarboxylation and hydroxylation of quinolone lead to the formation of by-product **2** (*m/z* 324). By-products **11** and **2** have been reported in previous studies on NOR degradation (Ding et al., 2017).

Another pathway of •OH attack on the quinolone group can be explained through the transformation of the N-ethyl side chain (Babić et al., 2013; Jin et al., 2019). The

proposed pathway for the formation of compound **10** (*m/z* 306) involves the oxidation of CH_3 and the subsequent removal of the CO group (-28 Da). Compound **8** (*m/z* 284) is generated from subsequent hydration and partial elimination reactions (-60 Da, corresponding to the CH_3COOH loss); defluorination of compound **8** gives rise to by-product **4** (*m/z* 264).

The simultaneous or successive attack of radicals on the piperazinyl and quinolone fraction groups leads to the formation of compounds **7** (*m/z* 225) and **14** (*m/z* 383). In this case, the by-product precursor **11** (of compound **14**), undergoes oxidative rearrangements in the piperazine group, resulting in (-14 Da) and C_2H_6 (-30 Da) groups. Regarding compound **7**, the rearrangement of the piperazine group, proposed for by-product **5,** is accompanied by oxidation reactions and the elimination of the COOH (-45 Da) and CO (-28 Da) groups from the quinolone ring.

3.6 Computational Simulations of NOR Degradation after the Radical Attack under the Photo-Electro-Fenton Process

Based on the simulations of the f^0 indices in solvated medium, we were able to obtain the results for these indices; the main values obtained can be found in Table 2 (the remaining values are presented in Table 3).

Based on the results presented in Table 2, one can analyze the regions of greater reactivity of NOR against radical attacks ($^{\bullet}OH$). By comparing the results of this analysis (NOR reactivity against radical attacks) with the experimental data obtained from mass spectrometry, one will observe that NOR molecule can have four degradation pathway options (Fig. 10A); this is certainly in line with the results observed previously.

Path 1 (blue arrows, first by-product derived from the addition of H_2O_2) can be analyzed based on the results of the calculations using the values of the C_{19} and C_{20} atoms and according to the f^0 values obtained. It is suggested that the H_{36} atom is initially replaced by the $^{\bullet}OH$ added in the mechanism (0.15). Subsequently, the C_{19}-C_{20} bond is

cleaved, and together with another $^{\bullet}OH$, the by-product *m/z* 354 is generated. For pathway 2 (yellow arrows, first by-product created by the addition of O^{+}), the results obtained from the Fukui indices show that, with a high f^0 value, the N_4 atom can contribute to a ring opening; furthermore, the value indicated for C_{14} also suggests that one of the reaction pathways involves the opening of the ring to which this atom is attached, and this leads to the formation of the by-product of *m/z* 336.

For pathway 3, the f^0 values also corroborate with the experimental results, as the positive value on the C_{22} atom indicates cleavage at the C_{22} and O_{40} bond (the experimental pathway in which the first by-product with *m/z* 304 is characterized by the removal of OH). The value of the Fukui index obtained for C_{15} indicates the removal of the F_1 atom and the second by-product (*m/z* 273) of this degradation pathway. Regarding pathway 4 (degradation pathway starting with the removal of CH_3 from NOR), the f^0 value (0.04) corresponding to the N6 atom may influence the cleavage of the C_{17}-C_{21} bond, thus corroborating with the results obtained by mass spectrometry (*m/z* 306). Thus, the computational simulations performed in this work, which were based on the application of the Fukui (f^0) indices, point to the possible pathways for the degradation of the NOR molecule; in addition, the theoretical results are found to corroborate with the experimental results obtained from mass spectrometry.

After obtaining the Fukui index values and analyzing the degradation pathway, the ECOSAR technique was used to analyze the aquatic toxicity of NOR and the by-products generated in the contaminant degradation process. First, the ECOSAR values obtained were classified according to a table proposed in the work of Reuschenbach et al. 2008 [39]. This table correlates the LC50 and EC50 values obtained in ECOSAR with the probable aquatic toxicity levels. Based on the Reuschenbach table, a molecule is considered very toxic if the value is less than or equal to 1 mgL^{-1}; it is toxic if the value

is greater than 1 and less than or equal to 10 mgL^{-1}; it is harmful if the value is greater than 10 and less than or equal to 100 mgL^{-1}; and it is not harmful (or it is unharmful) if the value is greater than 100 mgL^{-1}. Based on the data presented in Fig. 10B and Fig. 10C, one can analyze the values obtained and the acute and chronic toxicity levels, respectively.

Looking at the data, it can be observed that NOR only presents a not-harmful toxicity level for green algae and in chronic toxicity. Regarding the degradation pathway obtained via mass spectrometry, one will observe that for pathway 1 (*m/z* 354, 324, and 383), the three by-products exhibit toxic and harmful levels of acute and chronic toxicity in daphnid. For fish, the by-products *m/z* 354 and *m/z* 383 exhibit a not-harmful level of acute toxicity; in terms of chronic toxicity, the by-product *m/z* 354 is found to be toxic, while the other two by-products (*m/z* 324 and *m/z* 383) present harmful levels of chronic toxicity. Regarding green algae, the by-products *m/z* 354 and *m/z* 324 exhibit harmful levels of acute toxicity, while the by-product *m/z* 383 exhibits a not-harmful level of acute toxicity.

For pathway 2 (*m/z* 336, 279, and 225), it was noted that, regarding fish, the by-product m/z 336 exhibits a not-harmful level of acute toxicity, while the by-products *m/z* 279 and *m/z* 225 exhibit toxic and harmful levels of acute toxicity, respectively. When it comes to chronic toxicity, both m/z 336 and *m/z* 279 exhibit a not-harmful level of toxicity, while *m/z* 225 exhibits a harmful level of toxicity. For daphnids, the by-product *m/z* 336 exhibits a not-harmful level of acute toxicity, *m/z* 279 presents a toxic level of acute toxicity, and m/z 225 exhibits a harmful level of acute toxicity. Regarding daphnids, both the by-products *m/z* 336 and *m/z* 279 exhibit a not-harmful level of chronic toxicity, while *m/z* 225 exhibits a toxic level of chronic toxicity. For green algae, the degradation by-products generated via pathway 2 exhibit the following acute toxicity behavior: *m/z*

279 is not harmful, *m/z* 225 is toxic, and *m/z* 336 is harmful. For chronic toxicity in algae, the by-products *m/z* 336 and *m/z* 279 are not harmful, while the by-product *m/z* 225 is toxic.

Regarding the by-products of pathway 2.1 (*m/z* 318, 291, 273, 259), for acute toxicity in fish, the by-products *m/z* 318 and *m/z* 291 are found to be toxic, whereas the by-products *m/z* 273 and *m/z* 259 are found to be unharmful. For daphnids, the results obtained showed that all the four by-products are not harmful; for green algae, the following results were obtained: by-product *m/z* 318 is not harmful; by-product *m/z* 291 is toxic, and by-products *m/z* 273 and *m/z* 259 are harmful. For the analysis of chronic toxicity, the four by-products of pathway 2.1 are found to be unharmful in fish. For daphnids, the results obtained showed that the by-products m/z 318 and *m/z* 291 are harmful, while the by-products *m/z* 273 and 259 are not harmful. In the case of green algae, the results showed that the by-products *m/z* 273 and *m/z* 259 are very toxic, m/z 291 is toxic, and *m/z* 318 is not harmful. For the analysis of pathway 3, the results showed that both the by-products *m/z* 304 and *m/z* 273 exhibit a not harmful level of acute toxicity in fish; for daphnids, the by-product *m/z* 304 exhibits a harmful level of acute toxicity, while *m/z* 273 displays a not harmful level of acute toxicity. In the case of green algae, both the by-products *m/z* 304 and *m/z* 273 exhibit a harmful level of acute toxicity. For the analysis of chronic toxicity, the by-product *m/z* 273 is found to be unharmful in fish and daphnids, yet this same by-product is very toxic in green algae. However, the by-product *m/z* 304 exhibits a harmful level of chronic toxicity in fish and a toxic level of chronic toxicity in both daphnids and green algae.

Finally, regarding the by-products of pathway 4 (*m/z* 306, 284 and 264), for the analysis of acute toxicity, it was found that, for green algae, the three by-products are not harmful; for fish, the by-product *m/z* 306 is not harmful but the by-products *m/z* 284 and

m/z 264 are found to be toxic; for daphnids, the by-product *m/z* 306 is harmful, while the by-products *m/z* 284 and *m/z* 264 are not harmful. For the analysis of chronic toxicity, the by-products *m/z* 306 and *m/z* 264 are not harmful, while the by-product *m/z* 284 is harmful. The by-product *m/z* 306 exhibits a toxic level of chronic toxicity in daphnids, while m/z 284 and *m/z* 264 exhibit a harmful level of chronic toxicity. Finally, for green algae, the by-products *m/z* 284 and 264 exhibit a harmful level of chronic toxicity, while *m/z* 306 is toxic. Thus, based on the results obtained, one can observe that for fish, the most toxic by-products are *m/z* 354 (acute and chronic toxicity) and *m/z* 264 (acute toxicity); for daphnids, the by-products with the highest toxicity are *m/z* 225 (chronic toxicity), *m/z* 354 and *m/z* 324 (chronic toxicity), and *m/z* 304 (chronic toxicity); and for green algae, the molecules with the highest toxicity are *m/z* 273 (chronic toxicity), *m/z* 259 (chronic toxicity) and *m/z* 306 (chronic toxicity). The results also showed that the most toxic by-products are those associated with chronic toxicity.

4. CONCLUSION

The CaFeW NPs catalysts evaluated in this work demonstrated high catalytic properties when applied in Fenton, Photo-Fenton and Photo-Electro-Fenton processes for degradation of MB, FG dyes and NOR. The composition of $Ca_4Fe^{II}_{1.92}W_{0.08}Fe^{III}_4(PO_4)_6(OH)_2$ NPs exhibited the best results when applied as heterogeneous catalyst in the Photo-Electro-Fenton process; it recorded 100% discoloration of MB and FG dyes after 90 min. of electrolysis. However, when it comes to the analysis of mineralization, we observed the formation of recalcitrant by-products, which were recorded by HPLC-MS/MS. The application of optimized conditions under the Photo-Electro-Fenton process led to the complete degradation of NOR, where total removal of the molecule was obtained in 40 min., with mineralization rates of ~86%

recorded after 240 min. of treatment. The HPLC-MS/MS results obtained were found to be in agreement with the theoretical Fukui indices and the ECOSAR data recorded. Thus, based on the findings, one can conclude that the CaFeW NPs showed excellent synergy with the H_2O_2 electrogenerated *in situ* from the PCL6-GDE reactor. The application of the proposed catalyst led to the formation of a significant amount of •OH and others strong oxidizing species, evidenced by the high levels of mineralization obtained from the degradation of the contaminants evaluated.

ACKNOWLEDGEMENTS

The authors do warmly acknowledge the financial assistance provided by the Brazilian research funding agencies in support of this research: the Coordination for the Improvement of Higher Education Personnel – CAPES, the Brazilian National Council for Scientific and Technological Development – CNPq (grant #303943/2021-1) and the Sao Paulo State Foundation for the Support of Research – FAPESP (grant #2017/10118-0).

References

Al-Ahmed, Z.A., Al-Radadi, N.S., Ahmed, M.K., Shoueir, K., El-Kemary, M., 2020. Dye removal, antibacterial properties, and morphological behavior of hydroxyapatite doped with Pd ions. Arabian Journal of Chemistry 13, 8626–8637. https://doi.org/10.1016/j.arabjc.2020.09.049

Alburaih, H.A., Aman, S., Ahmad, N., Ejaz, S.R., Khosa, R.Y., Abid, A.G., Manzoor, S., Farid, H.M.T., Waheed, M.S., Taha, T.A., 2022. Synergistic photodegradation of methylene blue by Sm doped Fe2O3 photocatalyst under sunlight. Chinese Journal of Physics. https://doi.org/10.1016/j.cjph.2022.08.017

Avakyan, L., Paramonova, E., Bystrov, V., Coutinho, J., Gomes, S., Renaudin, G., 2021. Iron in hydroxyapatite: Interstitial or substitution sites? Nanomaterials 11, 1–19. https://doi.org/10.3390/nano11112978

Awais, M., Khursheed, S., Tehreem, R., Sirajuddin, Mok, Y.S., Siddiqui, G.U., 2022. pH regulated rapid photocatalytic degradation of methylene blue dye via niobium-nitrogen co-doped titanium dioxide nanostructures under sunlight. Applied Catalysis A: General 643, 118764. https://doi.org/10.1016/j.apcata.2022.118764

Babić, S., Periša, M., Škorić, I., 2013. Photolytic degradation of norfloxacin, enrofloxacin and ciprofloxacin in various aqueous media. Chemosphere 91, 1635–1642. https://doi.org/10.1016/j.chemosphere.2012.12.072

Barbaux, Y., Dekiouk, M., Le Maguer, D., Gengembre, L., Huchette, D., Grimblot, J., 1992. Bulk and surface analysis of a Fe-P-O oxydehydrogenation catalyst. Applied Catalysis A, General 90, 51–60. https://doi.org/10.1016/0926-860X(92)80247-A

Barros, W.R.P., Steter, J.R., Lanza, M.R.V., Tavares, A.C., 2016. Catalytic activity of Fe3-xCuxO4 ($0 \leq x \leq 0.25$) nanoparticles for the degradation of Amaranth food dye by heterogeneous electro-Fenton process. Applied Catalysis B: Environmental 180, 434–441. https://doi.org/10.1016/j.apcatb.2015.06.048

Bhuvanendran, N., Ravichandran, S., Xu, Q., Maiyalagan, T., Su, H., 2022. A quick guide to the assessment of key electrochemical performance indicators for the oxygen reduction reaction: A comprehensive review. Int J Hydrogen Energy 47, 7113–7138. https://doi.org/10.1016/j.ijhydene.2021.12.072

Bimbi Junior, F., Neves, C., do Nascimento, M., Falcão, E., Barros, W., 2022. Photo-Fenton-Based Degradation of Methylene Blue Dye Using Hydroxyapatite Nanoparticles Doped with Fe3O4/γ-Fe2O3. Journal of the Brazilian Chemical Society 00, 1–15. https://doi.org/10.21577/0103-5053.20220079

Boukha, Z., González-Prior, J., Rivas, B. de, González-Velasco, J.R., López-Fonseca, R., Gutiérrez-Ortiz, J.I., 2016. Synthesis, characterisation and behaviour of Co/hydroxyapatite catalysts in the oxidation of 1,2-dichloroethane. Applied Catalysis B: Environmental 190, 125–136. https://doi.org/10.1016/j.apcatb.2016.03.005

Brillas, E., 2022. Progress of homogeneous and heterogeneous electro-Fenton treatments of antibiotics in synthetic and real wastewaters. A critical review on the period 2017–2021. Science of the Total Environment 819, 153102. https://doi.org/10.1016/j.scitotenv.2022.153102

Carneiro, J.F., Aquino, J.M., Silva, B.F., Silva, A.J., Rocha-Filho, R.C., 2020. Comparing the electrochemical degradation of the fluoroquinolone antibiotics norfloxacin and ciprofloxacin using distinct electrolytes and a BDD anode: evolution of main oxidation byproducts and toxicity. Journal of Environmental Chemical Engineering 8. https://doi.org/10.1016/j.jece.2020.104433

Cawthray, J.F., Creagh, A.L., Haynes, C.A., Orvig, C., 2015. Ion exchange in hydroxyapatite with lanthanides. Inorganic Chemistry 54, 1440–1445. https://doi.org/10.1021/ic502425e

Chang, S.H., Jampang, A.O.A., 2023. Enhanced adsorption selectivity of Au(III) over Cu(II) from acidic chloride solutions by chitosan/palm kernel fatty acid distillate/magnetite nanocomposites. International Journal of Biological Macromolecules 252, 126491. https://doi.org/10.1016/j.ijbiomac.2023.126491

Coledam, D.A.C., Aquino, J.M., Silva, B.F., Silva, A.J., Rocha-Filho, R.C., 2016. Electrochemical mineralization of norfloxacin using distinct boron-doped diamond anodes in a filter-press reactor, with investigations of toxicity and oxidation by-products. Electrochimica Acta 213, 856–864. https://doi.org/10.1016/j.electacta.2016.08.003

Collins Arun Prakash, V., Venda, I., Thamizharasi, V., Sathya, E., 2020. A comparative study on microemulsion synthesis of hydroxyapatite powders by ionic and Non-Ionic surfactants. Materials Today: Proceedings. https://doi.org/10.1016/j.matpr.2020.10.026

Deng, X., Chen, R., Wang, C., Liang, Z., Zhao, Z., Shi, W., Cui, F., 2023. Iron-tungsten oxides modified oxygen-rich carbon nitride with defects S-scheme heterojunction for boosting photo-Fenton like removal of pollutants. Chemical Engineering Journal 451, 138629. https://doi.org/10.1016/j.cej.2022.138629

Ding, D., Liu, C., Ji, Y., Yang, Q., Chen, L., Jiang, C., Cai, T., 2017. Mechanism insight of degradation of norfloxacin by magnetite nanoparticles activated persulfate: Identification of radicals and degradation pathway. Chemical Engineering Journal 308, 330–339. https://doi.org/10.1016/j.cej.2016.09.077

Domingo-Torner, C., García-Gabaldón, M., Martí-Calatayud, M.C., Mestre, S., Pérez-Herranz, V., 2023. Norfloxacin mineralization under light exposure using Sb–SnO2 ceramic anodes coated with BiFeO3 photocatalyst. Chemosphere 313. https://doi.org/10.1016/j.chemosphere.2022.137518

Edralin, E.J.M., Garcia, J.L., dela Rosa, F.M., Punzalan, E.R., 2017. Sonochemical synthesis, characterization and photocatalytic properties of hydroxyapatite nano-rods derived from mussel shells. Materials Letters 196, 33–36. https://doi.org/10.1016/j.matlet.2017.03.016

Expósito, A.J., Monteagudo, J.M., Durán, A., Fernández, A., 2017. Dynamic behavior of hydroxyl radical in sono-photo-Fenton mineralization of synthetic municipal wastewater effluent containing antipyrine. Ultrasonics Sonochemistry 35, 185–195. https://doi.org/10.1016/j.ultsonch.2016.09.017

Ferri, M., Campisi, S., Scavini, M., Evangelisti, C., Carniti, P., Gervasini, A., 2019. In-depth study of the mechanism of heavy metal trapping on the surface of hydroxyapatite. Applied Surface Science 475, 397–409. https://doi.org/10.1016/j.apsusc.2018.12.264

Guinotte, F., Gautron, J., Nys, Y., Soumarmon, A., 1995. Calcium solubilization and retention in the gastrointestinal tract in chicks (Gallus domesticus) as a function of gastric acid secretion inhibition and of calcium carbonate particle size. British Journal of Nutrition 73, 125–139. https://doi.org/10.1079/bjn19950014

Hou, P., Shi, C., Wu, L., Hou, X., 2016. Chitosan/hydroxyapatite/Fe3O4 magnetic composite for metal-complex dye AY220 removal: Recyclable metal-promoted Fenton-like degradation. Microchemical Journal 128, 218–225. https://doi.org/10.1016/j.microc.2016.04.022

Ibrahim, M., Labaki, M., Giraudon, J.M., Lamonier, J.F., 2020. Hydroxyapatite, a multifunctional material for air, water and soil pollution control: A review. Journal of Hazardous Materials 383, 121139. https://doi.org/10.1016/j.jhazmat.2019.121139

Indrani, D.J., Soegijono, B., Adi, W.A., Trout, N., 2017. Phase composition and crystallinity of hydroxyapatite with various heat treatment temperatures. International Journal of Applied Pharmaceutics 9, 87–91. https://doi.org/10.22159/ijap.2017.v9s2.21

Jin, X., Zhou, X., Sun, P., Lin, S., Cao, W., Li, Z., Liu, W., 2019. Photocatalytic degradation of norfloxacin using N-doped TiO2: Optimization, mechanism, identification of intermediates and toxicity evaluation. Chemosphere 237. https://doi.org/10.1016/j.chemosphere.2019.124433

Kabir, S.F., Ahmed, S., Mustafa, A.I., Ahsan, M., Islam, S., 2012. Synthesis and Characterization of Fe-doped Hydroxyapatite. Bangladesh Journal of Scientific and Industrial Research 47, 1–8. https://doi.org/10.3329/bjsir.v47i1.10711

Khan, Idrees, Saeed, K., Zekker, I., Zhang, B., Hendi, A.H., Ahmad, A., Ahmad, S., Zada, N., Ahmad, H., Shah, L.A., Shah, T., Khan, Ibrahim, 2022. and Photodegradation.

Kirchon, A., Zhang, P., Li, J., Joseph, E.A., Chen, W., Zhou, H.C., 2020. Effect of Isomorphic Metal Substitution on the Fenton and Photo-Fenton Degradation of Methylene Blue Using Fe-Based Metal-Organic Frameworks. ACS Applied Materials and Interfaces 12, 9292–9299. https://doi.org/10.1021/acsami.9b21408

Kishor, R., Saratale, G.D., Saratale, R.G., Romanholo Ferreira, L.F., Bilal, M., Iqbal, H.M.N., Bharagava, R.N., 2021. Efficient degradation and detoxification of methylene blue dye by a newly isolated ligninolytic enzyme producing bacterium

Bacillus albus MW407057. Colloids and Surfaces B: Biointerfaces 206, 111947. https://doi.org/10.1016/j.colsurfb.2021.111947

Kosmulski, M., 2020. The pH dependent surface charging and points of zero charge. VIII. Update. Adv Colloid Interface Sci 275, 102064. https://doi.org/10.1016/j.cis.2019.102064

Krishna Murti, G.S.R., Moharir, A. V., Sarma, V.A.K., 1970. Spectrophotometric determination of iron with orthophenanthroline. Microchemical Journal 15, 585–589. https://doi.org/10.1016/0026-265X(70)90101-3

Kumar, P., Thakur, N., Kumar, K., Jeet, K., 2023. Photodegradation of methyl orange dye by using Azadirachta indica and chemically mediated synthesized cobalt doped α-Fe2O3 NPs through co-precipitation method. Materials Today: Proceedings. https://doi.org/10.1016/j.matpr.2023.01.257

Li, J., Ma, S., Qi, Z., Ding, J., Yin, M., Zhao, B., Zhang, Z., Wang, Y., Zhang, H., Wang, L., Dionysiou, D.D., 2023. Insights into the removal of chloramphenicol by electrochemical reduction on Pd/NiFe-MOF/foam-Ni electrode: Performance and mechanism. Applied Catalysis B: Environmental 322, 122076. https://doi.org/10.1016/j.apcatb.2022.122076

Liu, W., Qian, G., Zhang, B., Liu, L., Liu, H., 2016. Facile synthesis of spherical nano hydroxyapatite and its application in photocatalytic degradation of methyl orange dye under UV irradiation. Materials Letters 178, 15–17. https://doi.org/10.1016/j.matlet.2016.04.175

Liu, Y., Wang, X., Ye, W., Butenko, D.S., Lu, P., Chen, Q., Cai, R., Sun, J., Zhu, Y., Yang, D., 2022. FeOx nanoclusters decorated TiO2 for boosting white LED driven photocatalytic Fenton-like norfloxacin degradation. Separation and Purification Technology 303, 122194. https://doi.org/10.1016/j.seppur.2022.122194

Liu, Y., Zhao, Y., Wang, J., 2021. Fenton/Fenton-like processes with in-situ production of hydrogen peroxide/hydroxyl radical for degradation of emerging contaminants: Advances and prospects. Journal of Hazardous Materials 404, 124191. https://doi.org/10.1016/j.jhazmat.2020.124191

Lv, C., Jiao, P., Xin, H., Wu, L., Ouyang, G., Hou, X., 2024. Earth-abundant insulator hydroxyapatite-based composite for full-spectrum photocatalytic degradation of 2, 4- dichlorophenol. Applied Catalysis B: Environmental 340, 123248. https://doi.org/10.1016/j.apcatb.2023.123248

Ma, X., Liu, X., Zhang, X., Piao, C., Liu, Z., Fang, D., Wang, J., 2021. Construction of dual Z-scheme NiO/NiFe2O4/Fe2O3 photocatalyst via incomplete solid state chemical combustion reactions for organic pollutant degradation with simultaneous hydrogen production. International Journal of Hydrogen Energy 46, 31659–31673. https://doi.org/10.1016/j.ijhydene.2021.07.076

Mandavgane, S.A., 2020. Study of degradation of p-toluic acid by photo-oxidation, peroxidation, photo-peroxidation and photo-fenton processes. Materials Today: Proceedings 29, 1213–1216. https://doi.org/10.1016/j.matpr.2020.05.478

Marcus D Hanwell1, 2*, DonaldECurtis3, David C Lonie4, Tim Vandermeersch5, E.Z. and G.R.H., 2014. Avogadro: an advanced semantic chemical editor, visualization, and analysis platform. Advances in Mathematics 262, 476–483. https://doi.org/10.1016/j.aim.2014.05.019

Mishra, D., Arora, R., Lahiri, S., Amritphale, S.S., Chandra, N., 2014. Synthesis and characterization of iron oxide nanoparticles by solvothermal method. Protection of Metals and Physical Chemistry of Surfaces 50, 628–631. https://doi.org/10.1134/S2070205114050128

Mrunal, V.K., Vishnu, A.K., Momin, N., Manjanna, J., 2019. Cu2O nanoparticles for adsorption and photocatalytic degradation of methylene blue dye from aqueous medium. Environmental Nanotechnology, Monitoring and Management 12. https://doi.org/10.1016/j.enmm.2019.100265

Nagasaki, T., Nagata, F., Sakurai, M., Kato, K., 2017. Effects of pore distribution of hydroxyapatite particles on their protein adsorption behavior. Journal of Asian Ceramic Societies 5, 88–93. https://doi.org/10.1016/j.jascer.2017.01.005

Nidheesh, P.V., Trellu, C., Vargas, H.O., Mousset, E., Ganiyu, S.O., Oturan, M.A., 2023. Electro-Fenton process in combination with other advanced oxidation processes: Challenges and opportunities. Current Opinion in Electrochemistry 37, 101171. https://doi.org/10.1016/j.coelec.2022.101171

Pai, S., Kini, M.S., Selvaraj, R., 2021. A review on adsorptive removal of dyes from wastewater by hydroxyapatite nanocomposites. Environmental Science and Pollution Research 28, 11835–11849. https://doi.org/10.1007/s11356-019-07319-9

Patel, S., Wei, S., Han, J., Gao, W., 2015. Transmission electron microscopy analysis of hydroxyapatite nanocrystals from cattle bones. Materials Characterization 109, 73–78. https://doi.org/10.1016/j.matchar.2015.09.019

Plater, M.J., 2003. A degradation product of methylene blue. Arkivoc 2003, 37–42. https://doi.org/10.3998/ark.5550190.0004.105

Qutob, M., Hussein, M.A., Alamry, K.A., Rafatullah, M., 2022. A review on the degradation of acetaminophen by advanced oxidation process: pathway, by-products, biotoxicity, and density functional theory calculation. RSC Advances 12, 18373–18396. https://doi.org/10.1039/d2ra02469a

Raducan, A., Bogdan, D., Galaon, T., Oancea, P., 2022. Oxidative removal of Fast Green FCF and ponceaux 4R dyes by H2O2/NaHCO3, UV and H2O2/UV processes: A comparative study. Journal of Photochemistry and Photobiology A: Chemistry 431, 114040. https://doi.org/10.1016/j.jphotochem.2022.114040

Ragab, A., Ahmed, I., Bader, D., 2019. The removal of Brilliant Green dye from aqueous solution using nano hydroxyapatite/chitosan composite as a sorbent. Molecules 24. https://doi.org/10.3390/molecules24050847

Rasskazova, L.A., Zhuk, I. V., Korotchenko, N.M., Brichkov, A.S., Chen, Y.W., Paukshtis, E.A., Ivanov, V.K., Kurzina, I.A., Kozik, V. V., 2019. Synthesis of

Magnesium- and Silicon-modified Hydroxyapatites by Microwave-Assisted Method. Scientific Reports 9, 1–10. https://doi.org/10.1038/s41598-019-50777-x

Reuschenbach, P., Silvani, M., Dammann, M., Warnecke, D., Knacker, T., 2008. ECOSAR model performance with a large test set of industrial chemicals. Chemosphere 71, 1986–1995. https://doi.org/10.1016/j.chemosphere.2007.12.006

Saber-Samandari, Samaneh, Saber-Samandari, Saeed, Nezafati, N., Yahya, K., 2014. Efficient removal of lead (II) ions and methylene blue from aqueous solution using chitosan/Fe-hydroxyapatite nanocomposite beads. Journal of Environmental Management 146, 481–490. https://doi.org/10.1016/j.jenvman.2014.08.010

Sánchez-Montes, I., Fuzer Neto, J.R., Silva, B.F., Silva, A.J., Aquino, J.M., Rocha-Filho, R.C., 2018. Evolution of the antibacterial activity and oxidation intermediates during the electrochemical degradation of norfloxacin in a flow cell with a PTFE-doped β-PbO2 anode: Critical comparison to a BDD anode. Electrochimica Acta 284, 260–270. https://doi.org/10.1016/j.electacta.2018.07.122

Singh, A., Kumar, R.S., Gumpu, M.B., Zsuzsanna, L., Veréb, G., Kertész, S., Arthanareeswaran, G., 2020. Titanium dioxide doped hydroxyapatite incorporated photocatalytic membranes for the degradation of chloramphenicol antibiotic in water. Journal of Chemical Technology & Biotechnology. https://doi.org/10.1002/jctb.6617

Sithole, R.K., Machogo, L.F.E., Moloto, M.J., Gqoba, S.S., Mubiayi, K.P., Van Wyk, J., Moloto, N., 2020. One-step synthesis of Cu3N, Cu2S and Cu9S5 and photocatalytic degradation of methyl orange and methylene blue. Journal of Photochemistry and Photobiology A: Chemistry 397, 112577. https://doi.org/10.1016/j.jphotochem.2020.112577

Tampieri, A., D'Alessandro, T., Sandri, M., Sprio, S., Landi, E., Bertinetti, L., Panseri, S., Pepponi, G., Goettlicher, J., Bañobre-López, M., Rivas, J., 2012. Intrinsic magnetism and hyperthermia in bioactive Fe-doped hydroxyapatite. Acta Biomaterialia 8, 843–851. https://doi.org/10.1016/j.actbio.2011.09.032

Uskoković, V., 2020. X-ray photoelectron and ion scattering spectroscopic surface analyses of amorphous and crystalline calcium phosphate nanoparticles with different chemical histories. Physical Chemistry Chemical Physics 22, 5531–5547. https://doi.org/10.1039/c9cp06529f

Valizadeh, S., Rasoulifard, M.H., Seyed Dorraji, M.S., 2014. Modified Fe3O 4 - hydroxyapatite nanocomposites as heterogeneouscatalysts in three UV, Vis and Fenton like degradation system. Applied Surface Science 319, 358–366. https://doi.org/10.1016/j.apsusc.2014.07.139

Vlahović, F., Ognjanović, M., Djurdjić, S., Kukuruzar, A., Antić, B., Dojčinović, B., Stanković, D., 2023. Design of an ethidium bromide control circuit supported by deep theoretical insight. Applied Catalysis B: Environmental 334. https://doi.org/10.1016/j.apcatb.2023.122819

Wang, B., Wang, T., Su, H., 2022. A dye-methylene blue (MB)-degraded by hydrodynamic cavitation (HC) and combined with other oxidants. Journal of Environmental Chemical Engineering 10, 107877. https://doi.org/10.1016/j.jece.2022.107877

Wang, C., Yu, G., Chen, H., Wang, J., 2021. Degradation of norfloxacin by hydroxylamine enhanced fenton system: Kinetics, mechanism and degradation pathway. Chemosphere 270. https://doi.org/10.1016/j.chemosphere.2020.129408

Wang, M., Zhang, K., Wu, M., Wu, Q., Liu, J., Yang, J., Zhang, J., 2019. Unexpectedly High Adsorption Capacity of Esterified Hydroxyapatite for Heavy Metal Removal. Langmuir 35, 16111–16119. https://doi.org/10.1021/acs.langmuir.9b02373

Wei, H., Meng, F., Zhang, H., Yu, W., Li, J., Yao, S., 2024. Novel oxygen vacancy-rich Bi2MoO6-SOVs/MgFe2O4 S-scheme heterojunction piezo-photocatalytic for efficient degradation of norfloxacin and theoretical calculations. Chemical Engineering Journal 479, 147738. https://doi.org/10.1016/j.cej.2023.147738

Yew, Y.P., Shameli, K., Miyake, M., Kuwano, N., Bt Ahmad Khairudin, N.B., Bt Mohamad, S.E., Lee, K.X., 2016. Green Synthesis of Magnetite (Fe3O4) Nanoparticles Using Seaweed (Kappaphycus alvarezii) Extract. Nanoscale Research Letters 11. https://doi.org/10.1186/s11671-016-1498-2

Youness, R.A., Taha, M.A., Elhaes, H., Ibrahim, M., 2017. Molecular modeling, FTIR spectral characterization and mechanical properties of carbonated-hydroxyapatite prepared by mechanochemical synthesis. Materials Chemistry and Physics 190, 209–218. https://doi.org/10.1016/j.matchemphys.2017.01.004

Zhang, M., Niu, Y., Xu, Y., 2020. Heterogeneous Fenton-like magnetic nanosphere coated with vanadium oxide quantum dots for enhanced organic dyes decolorization. Journal of Colloid and Interface Science 579, 269–281. https://doi.org/10.1016/j.jcis.2020.06.067

Zhang, W., Bian, Z., Xin, X., Wang, L., Geng, X., Wang, H., 2021. Comparison of visible light driven H2O2 and peroxymonosulfate degradation of norfloxacin using Co/g-C3N4. Chemosphere 262, 127955. https://doi.org/10.1016/j.chemosphere.2020.127955

Zhou, P., Zhang, J., Zhang, G., Li, W., Liu, Yang, Cheng, X., Huo, X., Liu, Yunxin, Zhang, Y., 2019. Degradation of dimethyl phthalate by activating peroxymonosulfate using nanoscale zero valent tungsten: Mechanism and degradation pathway. Chemical Engineering Journal 359, 138–148. https://doi.org/10.1016/j.cej.2018.11.123

Figure 1. HRTEM images of Ca40Fe60W NPs at **(A)** bright field; **(A1)** dark field; **(A2)** EDS mapping and (**B** and **B1**) analysis of crystallographic planes and TEM images of **(C)** Ca40Fe60W, **(D)** Ca30Fe70W, **(E)** Ca25Fe75W and **(F)** Ca0Fe100W NPs.

Figure 2. High–resolution XPS spectra of O 1s, P 2p, and Fe 2p regions for **(A)** Ca40Fe60W, **(B)** Ca30Fe70W, **(C)** Ca25Fe75W and **(D)** Ca0Fe100W NPs

Figure 3. (A-B) MB dye color removal and **(C-D)** mineralization rate after 120 min. of degradation by photo-electro-Fenton process using Ca40Fe60W NPs (0.06 g), 0.1 mol L^{-1} K_2SO_4 as electrolyte and current densities of **(A-C)** 10 and **(B-D)** 20 mA cm^{-2} at pH 2.5; 7.0 and 9.0.

Figure. 4. (A-B) FG dye color removal and **(C-D)** mineralization rate after 120 min. of degradation by photo-electro-Fenton process using Ca40Fe60W NPs (0.06 g), 0.1 mol L^{-1} K_2SO_4 as electrolyte and current densities of **(A-C)** 10 and **(B-D)** 20 mA cm^{-2} at pH 2.5; 7.0 and 9.0.

Figure 5. (A) NOR removal, **(B)** mineralization rate after degradation by photo-electro-Fenton process at pH 2.5 using Ca40Fe60W NPs (0.06 g), 0.1 mol L^{-1} K_2SO_4 as electrolyte and current density of 10 mA cm^{-2} and **(C)** recyclability tests of Ca40Fe60W NPs on photo-electro-Fenton process NOR degradation.

Figure 6. (A) Possible photo-electro-Fenton degradation pathway to NOR according to the f^0 index. Theoretical estimation of **(B)** acute and **(C)** chronic toxicity for the NOR and the by-products related to the four degradation pathways. (VT: very toxic; T: toxic; H: harmful and NT: not-harmful).

Fig. 1

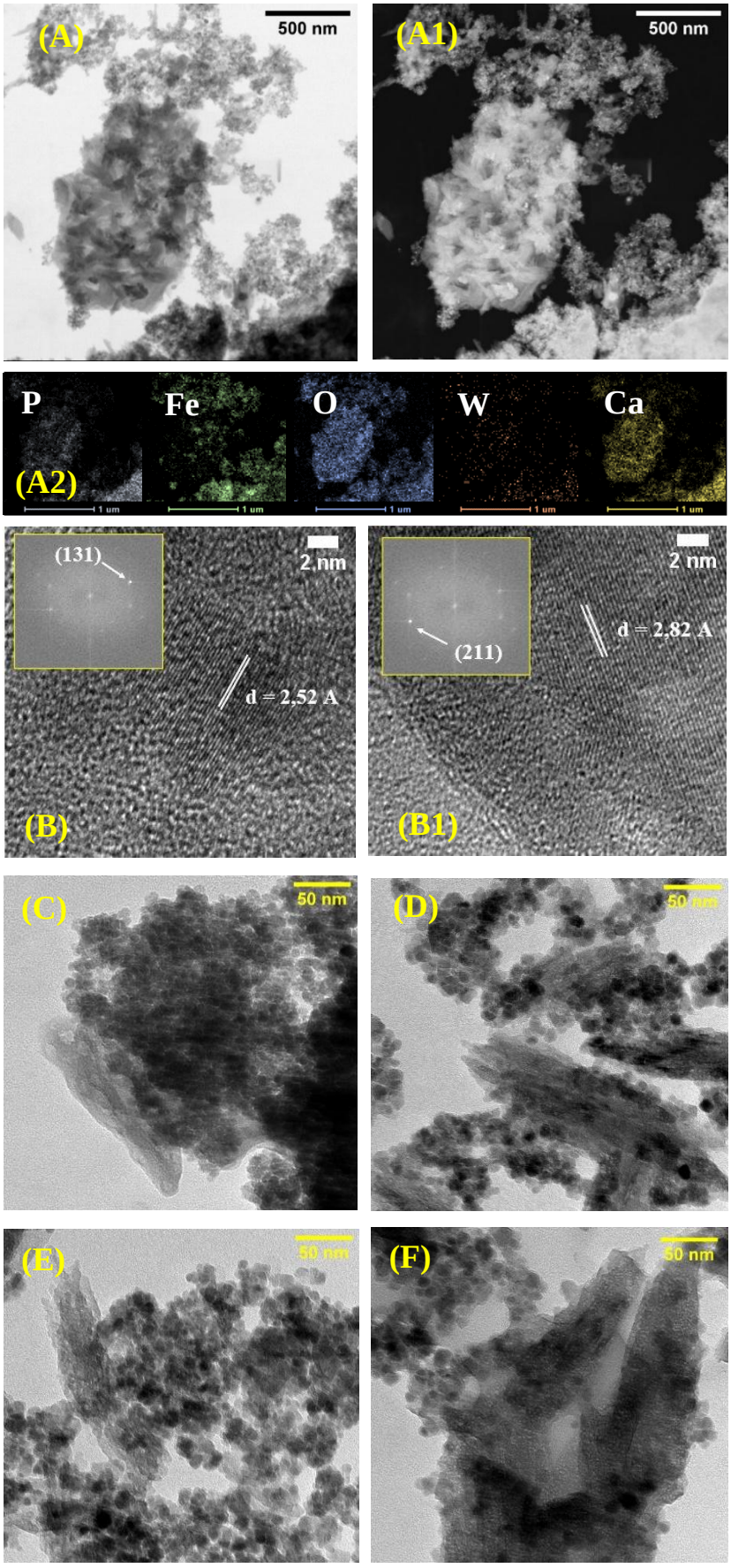
(A)
500 nm
(A1)
500 nm
P
Fe
O
W
Ca
(A2)
(131)
2 nm
d = 2.52 A
(B)
(211)
2 nm
d = 2.82 A
(B1)
(C)
50 nm
(D)
50 nm
(E)
50 nm
(F)
50 nm

Fig. 2.

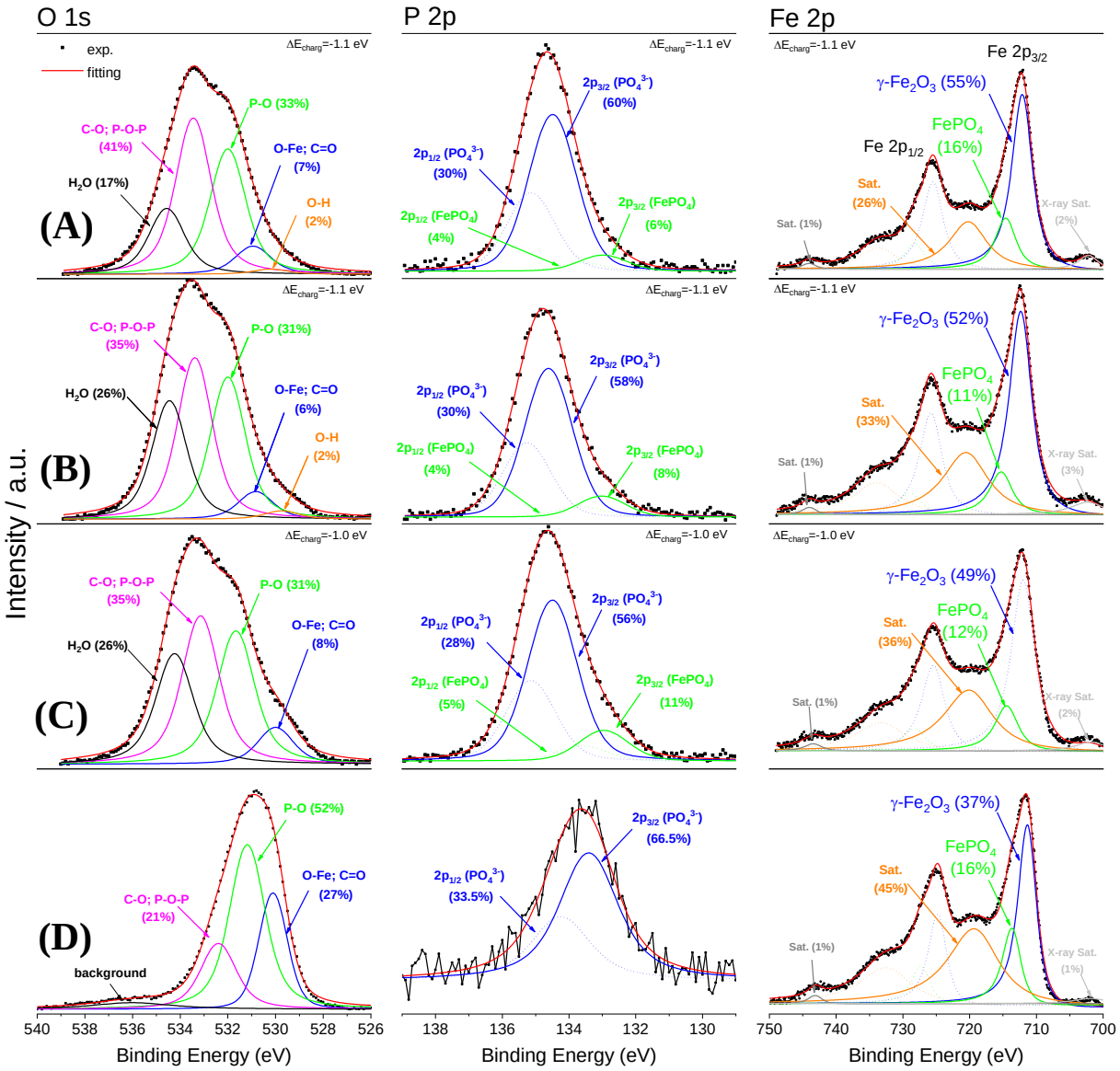
O 1s
P 2p
Fe 2p
exp.
fitting
ΔE_charg=-1.1 eV
ΔE_charg=-1.0 eV
C-O; P-O-P (41%)
P-O (33%)
O-Fe; C=O (7%)
H2O (17%)
O-H (2%)
(A)
C-O; P-O-P (35%)
P-O (31%)
O-Fe; C=O (6%)
H2O (26%)
O-H (2%)
(B)
C-O; P-O-P (35%)
P-O (31%)
O-Fe; C=O (8%)
H2O (26%)
(C)
P-O (52%)
O-Fe; C=O (27%)
C-O; P-O-P (21%)
background
(D)
2p3/2 (PO4 3-) (60%)
2p1/2 (PO4 3-) (30%)
2p1/2 (FePO4) (4%)
2p3/2 (FePO4) (6%)
2p3/2 (PO4 3-) (58%)
2p1/2 (PO4 3-) (30%)
2p1/2 (FePO4) (4%)
2p3/2 (FePO4) (8%)
2p3/2 (PO4 3-) (56%)
2p1/2 (PO4 3-) (28%)
2p1/2 (FePO4) (5%)
2p3/2 (FePO4) (11%)
2p3/2 (PO4 3-) (66.5%)
2p1/2 (PO4 3-) (33.5%)
Fe 2p3/2
γ-Fe2O3 (55%)
FePO4 (16%)
Fe 2p1/2
Sat. (26%)
Sat. (1%)
X-ray Sat. (2%)
γ-Fe2O3 (52%)
FePO4 (11%)
Sat. (33%)
Sat. (1%)
X-ray Sat. (3%)
γ-Fe2O3 (49%)
FePO4 (12%)
Sat. (36%)
Sat. (1%)
X-ray Sat. (2%)
γ-Fe2O3 (37%)
FePO4 (16%)
Sat. (45%)
Sat. (1%)
X-ray Sat. (1%)
Intensity / a.u.
540 538 536 534 532 530 528 526
138 136 134 132 130
750 740 730 720 710 700
Binding Energy (eV)
Binding Energy (eV)
Binding Energy (eV)

Fig. 3.

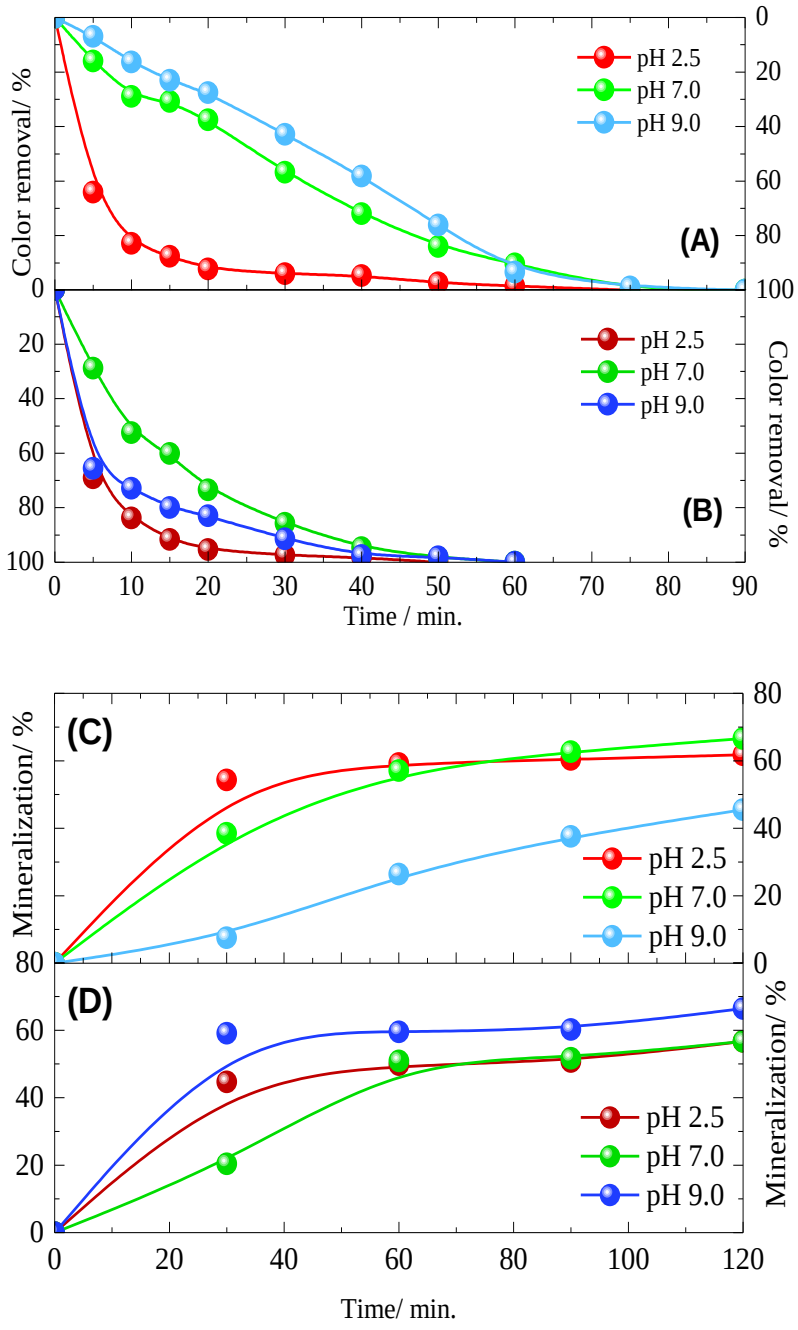
Color removal/ %
pH 2.5
pH 7.0
pH 9.0
(A)
(B)
Color removal/ %
Time / min.
Mineralization/ %
(C)
(D)
Mineralization/ %
Time/ min.

Fig. 4.

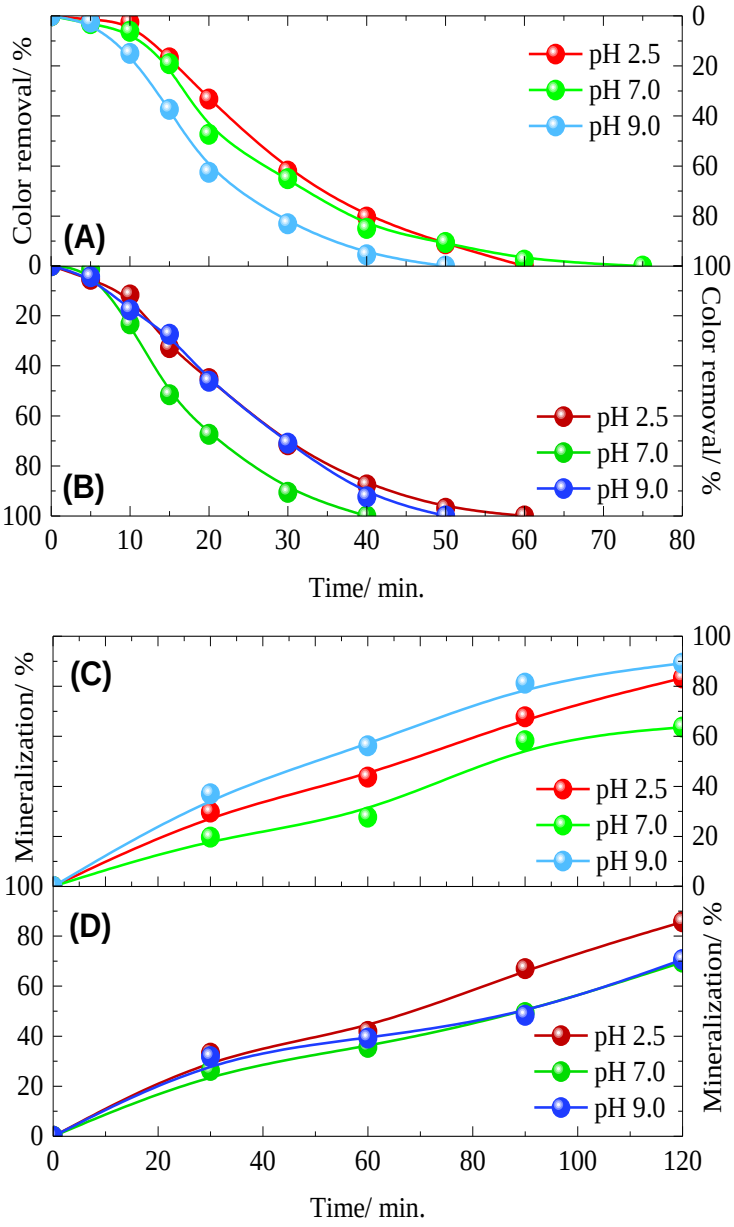
Color removal/ %
(A)
pH 2.5
pH 7.0
pH 9.0
(B)
Color removal/ %
Time/ min.
Mineralization/ %
(C)
(D)
Mineralization/ %
Time/ min.

Fig. 5.

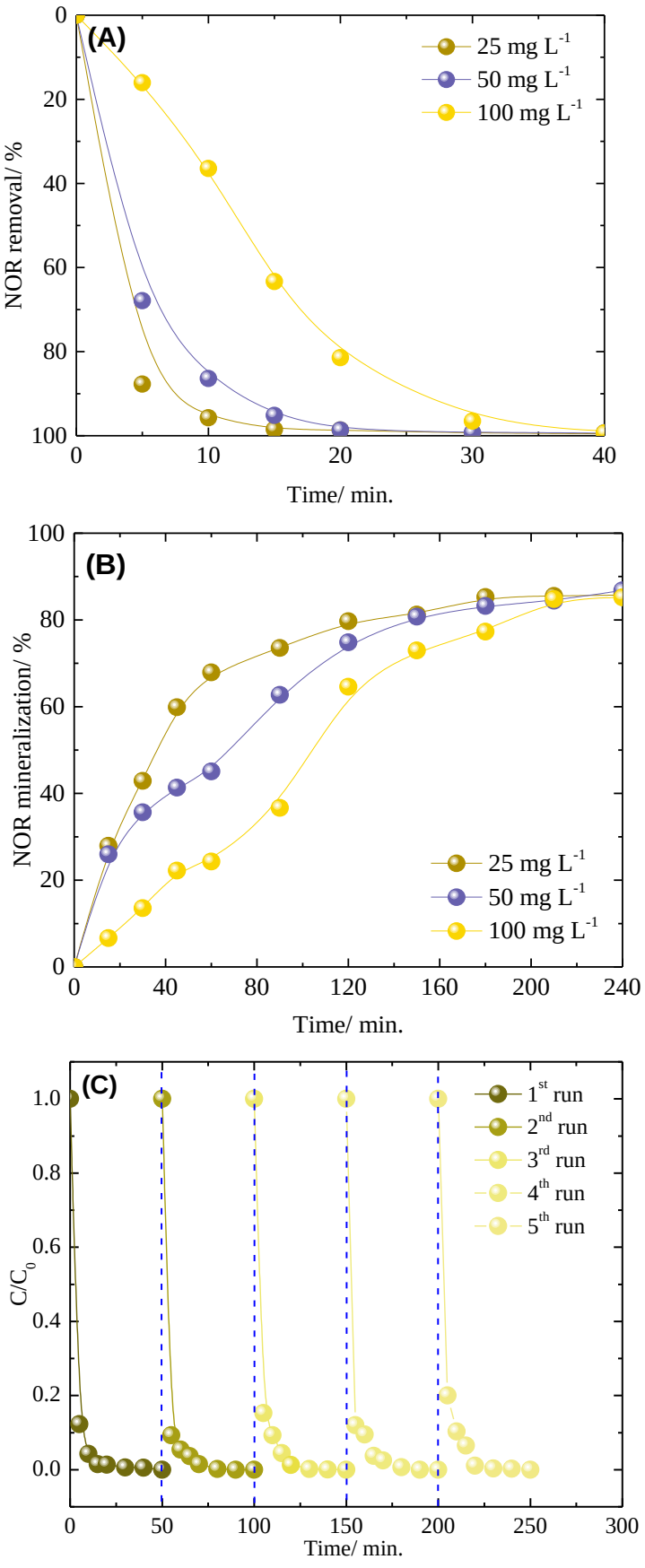
(A)
25 mg L-1
50 mg L-1
100 mg L-1
NOR removal/ %
Time/ min.
(B)
NOR mineralization/ %
Time/ min.
(C)
1st run
2nd run
3rd run
4th run
5th run
C/C0
Time/ min.

Fig. 6.

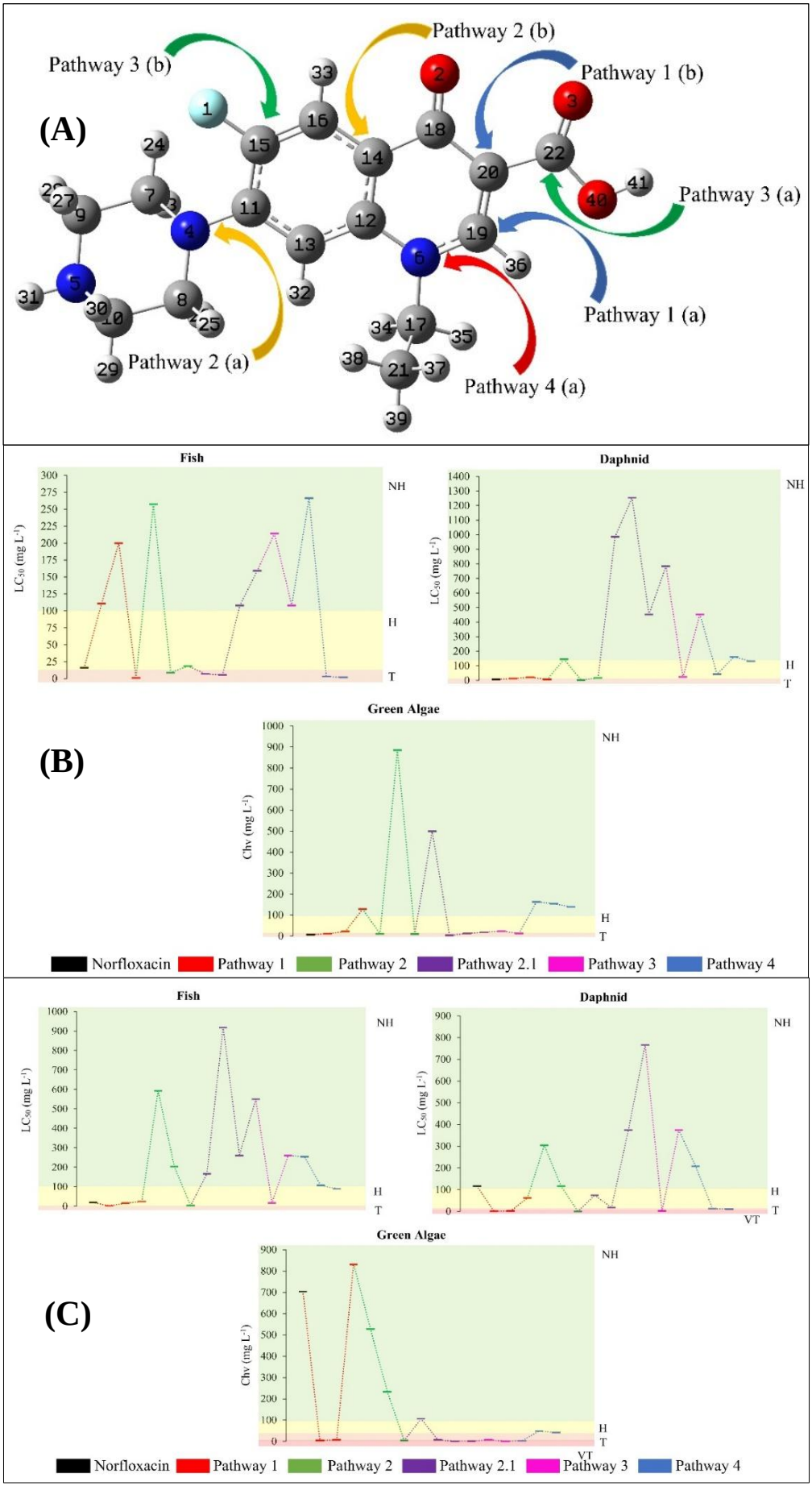
(A)
Pathway 3 (b)
Pathway 2 (b)
Pathway 1 (b)
Pathway 3 (a)
Pathway 1 (a)
Pathway 2 (a)
Pathway 4 (a)
(B)
Fish
Daphnid
Green Algae
LC50 (mg L-1)
Chv (mg L-1)
NH
H
T
(C)
VT
Norfloxacin
Pathway 1
Pathway 2
Pathway 2.1
Pathway 3
Pathway 4

Table 1. Charges of species q_N, q_{N+1}, q_{N-1} and the Fukui index f^0 for all atoms for NOR molecule in a solvated medium (water).

Atom	q_N	q_{N+1}	q_{N-1}	f^0
F_1	-0.35	-0.37	-0.32	0.02
O_2	-0.67	-0.76	-0.62	0.07
O_3	-0.65	-0.71	-0.64	0.03
N_4	-0.52	-0.54	-0.14	0.20
N_5	-0.74	-0.74	-0.74	0.00
N_6	-0.38	-0.43	-0.36	0.04
C_7	-0.26	-0.26	-0.30	-0.02
C_8	-0.27	-0.26	-0.32	-0.03
C_9	-0.27	-0.27	-0.28	0.00
C_{10}	-0.27	-0.27	-0.25	0.01
C_{11}	0.19	0.16	0.12	-0.02
C_{12}	0.21	0.21	0.16	-0.03
C_{13}	-0.31	-0.35	-0.17	0.09
C_{14}	-0.18	-0.21	-0.04	0.09
C_{15}	0.36	0.30	0.45	0.07
C_{16}	-0.22	-0.27	-0.23	0.02
C_{17}	-0.26	-0.25	-0.27	-0.01
C_{18}	0.53	0.49	0.52	0.02
C_{19}	0.14	-0.12	0.18	0.15
C_{20}	-0.33	-0.40	-0.34	0.03
C_{21}	-0.69	-0.69	-0.69	0.00
C_{22}	0.81	0.78	0.83	0.03
H_{23}	0.22	0.22	0.29	0.03
H_{24}	0.26	0.25	0.28	0.01
H_{25}	0.25	0.25	0.28	0.02
H_{26}	0.22	0.21	0.28	0.03
H_{27}	0.21	0.21	0.23	0.01
H_{28}	0.24	0.24	0.26	0.01
H_{29}	0.24	0.24	0.26	0.01
H_{30}	0.21	0.21	0.23	0.01
H_{31}	0.41	0.41	0.42	0.01
H_{32}	0.26	0.25	0.28	0.02
H_{33}	0.28	0.26	0.30	0.02
H_{34}	0.25	0.24	0.26	0.01
H_{35}	0.26	0.25	0.27	0.01
H_{36}	0.27	0.23	0.28	0.02
H_{37}	0.24	0.24	0.25	0.01
H_{38}	0.24	0.23	0.24	0.00
H_{39}	0.25	0.24	0.26	0.01
O_{40}	-0.75	-0.76	-0.74	0.01
H_{41}	0.54	0.53	0.54	0.01